FSI simulations of wind gusts impacting an air-inflated flexible membrane at Re = 100,000

Guillaume de Nayer, Michael Breuer, Khaled Boulbrachene

Journal of Fluids and Structures 109 (2022) 103462

Contents lists available at ScienceDirect

Journal of Fluids and Structures

journal homepage: www.elsevier.com/locate/jfs

FSI simulations of wind gusts impacting an air-inflated flexible membrane at Re = 100,000

G. De Nayer, M. Breuer *, K. Boulbrachene

Professur für Strömungsmechanik, Helmut-Schmidt-Universität Hamburg, D-22043 Hamburg, Germany

ARTICLE INFO

Article history:
Received 13 July 2021
Received in revised form 26 November 2021
Accepted 3 December 2021
Available online 28 December 2021

Keywords:
Wind gust
Fluid–structure interaction (FSI)
Hemisphere
Membrane
Turbulent flow
Large-eddy simulation (LES)
Source-term formulation

ABSTRACT

The paper addresses the simulation of turbulent wind gusts hitting rigid and flexible structures. The purpose is to show that such kind of complex fluid–structure interaction (FSI) problems can be simulated by high-fidelity numerical techniques with reasonable computational effort. The main ingredients required for this objective are an efficient method to inject wind gusts within the computational domain by the application of a recently developed source-term formulation, an equally effective method to prescribe the incoming turbulent flow and last but not least a reliable FSI simulation methodology to predict coupled problems based on a partitioned solution approach combining an LES fluid solver with a FEM/IGA solver for the structure. The present application is concerned with a rigid and a membranous hemisphere installed in a turbulent boundary layer and impacted by wind gusts of different strength. The methodology suggested allows to inject the gusts in close vicinity of the object of interest, which is typically well resolved. Therefore, the launch and transport of the wind gust can be realized without visible numerical dissipation and without large computational effort. The effect of the gusts on the flow field, the resulting forces on the structure and the corresponding deformations in case of the flexible structure are analyzed in detail. A comparison between the rigid and the flexible case makes it possible to work out the direct reaction of the deformations on the force histories during the impact. Furthermore, in case of the flexible structure the temporal relationships between local or global force developments and the local deformations are evaluated. Such predictions pinpoint the areas of high stresses and strains, where the material is susceptible to failure.

1. Introduction

Fluid–structure interaction (FSI) problems constitute a category of problems belonging to interdisciplinary subjects which have drawn the interest of scientists due to its crucial relevance to many industrial and practical applications. The fields in which these applications are found include aeronautics (e.g., wings), wind engineering (e.g., wind turbines), civil engineering (bridges, skyscrapers and lightweight thin structures) and even biomedical engineering (e.g., cardiac valves).

Among the wide range of applications, this work concentrates on the interaction of fluid flows with flexible membranous structures. Such structures have become widely used in the modern civil engineering industry due to their practical characteristics. Large expanses of space could be optimally enclosed by such structures as they are solely subjected to tensile membrane loads. They are also featured by their formability enabling the creative minds to come up with designs

* Corresponding author.
E-mail address: breuer@hsu-hh.de (M. Breuer).

https://doi.org/10.1016/j.jfluidstructs.2021.103462

which were not feasible with traditional construction materials while maintaining a cost-efficient solution. In a structure of this type, a pre-stress defining its shape and tensile state is required. For a tensile membrane structure, a pre-stress is imposed by the unique selection of boundary conditions, whereas for an air-inflated structure, a pre-stress is imposed by internal pressurized air. A careful consideration of this design parameter is necessary since it determines the stability and the integrity of a structure undergoing an interaction with different wind load scenarios. To this end, a realistic modeling of wind loads acting on this structure becomes mandatory to achieve reliable structural designs (Newman et al., 1984).

In nature, most extreme wind events are characterized by being non-stationary and highly transient (e.g., thunderstorms, tornados or wind gusts). The physics associated with convective gusts (e.g., winds spawned by thunderstorms) is fundamentally different from that involving conventional momentum driven turbulence (e.g., winds in neutrally stable atmospheric boundary layers) in both, kinematics and dynamics. The main distinguishing aspects are the dissimilar velocity profiles and the distinct statistical behavior (Kwon and Kareem, 2013).

In contrast to traditional logarithmic or power-law velocity profiles developing in an atmospheric boundary layer, the presence of a gust yields an inverted velocity profile with a peak value near the surface. Such a variation in the velocity profile certainly leads to a considerable change in the interaction between the fluid and the structure. This change could be further compounded by an increase in the parameters of the inherently transient gusts studied (i.e., gust amplitude and length scales). Moreover, a careful examination of the statistical nature of such extreme wind events is required. Typically, design wind loads are estimated based on a velocity profile (depending on the terrain category) evaluated by superimposing a mean wind velocity profile and gust-induced fluctuations characterized by a statistically stationary process. This assumption is, however, highly questionable as in the event of a wind gust, sharp changes in the wind speed are pronounced (Kareem and Wu, 2013).

Although design standards are established providing guidelines to prevent structural damages due to wind from happening (c.f., American Society of Civil Engineers, 1997; Frost et al., 1978; IEC-Standard, 2002; Burton et al., 2001; Kasperski, 2007), these are based on assumptions to alleviate the efforts of the design process. Therefore, the development of methods that help in establishing a framework for investigating the effect of realistic wind loads (transient, highly dynamic wind events), which significantly affect the structural response, would substantially contribute to the design procedure. Highly resolved numerical simulations of the flow field and the resulting deformations are seen as an effective tool to gain a deeper insight into the complex physics involved in such problems (Michalski et al., 2011, 2015).

The available literature concerned with the numerical simulation of the FSI problem comprising the evaluation of wind effects on flexible structures is vast and includes a wide range of applications. In the course of demonstrating the reliability of the coupling algorithm employed for conducting FSI simulations, Glück et al. (2003) simulated unsteady deformations of a membranous roof exposed to a basic flow superimposed by a time-dependent wind gust at the top inlet boundary. In Wüchner et al. (2007), transient FSI simulations were carried out and the maximum inflow wind speed was varied in a periodic manner to imitate the effect of a gust on a four-point membranous tent. Wu et al. (2008) investigated the interaction between the flow over a two-dimensional low-rise building and its flexible membranous roof. The inflow of the considered configuration was defined by a power law and the FSI dominant factors were highlighted by modifying flow and structural parameters. The results of the flexible case were analyzed and compared to its rigid counterpart. Yuan et al. (2010) carried out FSI simulations to describe the dynamic response of a flexible liquid-storage container under strong wind actions. A penalty based finite-element method combined with the Arbitrary Lagrangian–Eulerian description was used to solve the FSI problem. Several turbulent wind cases were accomplished and design recommendations were provided. The relevant studies of Michalski et al. (2011, 2015) simulated the structural response of a large membranous umbrella subjected to transient wind loads, where the effects of the gust were implicitly incorporated in the synthetically generated wind field. The study was supplemented by a statistical validation of the numerical methodology adopted based on a real-scale experimental setup. Augier et al. (2012) provided a quantitative experimental validation of a dynamic FSI model devoted to simulate the aeroelastic problem of yacht sails and rig. The FSI model coupled an inviscid flow solver based on the vortex-lattice method with a finite-element method based structural solver. The experimental and numerical results of the flying shapes of the sails and the loads on the rigs showed good agreement. Mokin et al. (2017) simulated the aeroelastic behavior of an air-supported structure by a monolithic and a partitioned approach. An inflated shell in form of a clipped 3/4 sphere with a prescribed internal pressure was subjected to an air flow of high Reynolds number to mimic the wind interaction during storms. Results of different wind speeds were compared against experimental data and a good agreement was achieved. In the scope of the recent advancements in the prediction of the aeroelastic response of wind turbines, Santo et al. (2020) carried out high-fidelity FSI simulations of a horizontal-axis wind turbine immersed in an atmospheric boundary layer based on the RANS approach. Wind gusts of different shapes and strengths were modeled and superimposed on the atmospheric boundary layer to locally impact a single blade when pointing upwards. The loads and deflections of the blade were monitored through its rotation.

Despite the extensive FSI studies conducted, it can be stated that according to the best knowledge of the authors, no study had an emphasis on the dynamic effects of an explicitly defined local wind gusts on flexible membranous structures. For this purpose, this work focuses on establishing a computational FSI framework to assess the effect of a wind gust convecting through a turbulent boundary layer and impacting on an air-inflated spherically shaped flexible membranous structure. The present test case is a further development step of two subsequent setups. In Wood et al. (2016) the flow around a rigid hemisphere placed within a turbulent boundary layer was studied experimentally and numerically. In Wood et al. (2018) the rigid hemisphere was replaced by a flexible membrane with nominally the same

shape and experimentally studied in the same wind tunnel as the rigid counterpart before. This FSI test case was also studied in detail based on coupled numerical simulations in De Nayer et al. (2018a) and Apostolatos et al. (2019a). The new contribution here is that the turbulent inflow is now superimposed by a wind gust in order to investigate the effect of such short-term but strong phenomena on the forces and deformations of the structure.

The paper is organized as follows: In Section 2, the source-term wind gust modeling technique employed for the injection of the wind gust inside the computational domain is presented. Section 3 describes the numerical framework applied to solve the FSI problem. Section 4 and Section 5 provide the details about the computational setup of the rigid and the flexible hemisphere followed by a description of the applied wind gusts parameters in Section 6. The results obtained for different wind gusts on the rigid and flexible case are discussed in Section 7 and summarized in Section 8.

2. Wind gust modeling

2.1. Overview

Modeled wind gust profiles can be classified into two main categories, namely, deterministic and stochastic wind gusts. The scope of this work is restricted to deterministic gusts relying on the superposition of an analytical function defining the mean shape of the gust and synthetically generated turbulence. In the literature, there exist different alternatives for the injection of wind gusts into the computational domains. One of the conventional approaches is referred to as the far-field boundary condition (FBC) method, where the wind gust is introduced at the inlet patch and can freely propagate through the domain (Norris et al., 2010). The gust is, however, susceptible to numerical dissipation owing to the often coarse grid resolution in the upstream region. As a remedy, a fine overset grid is often used to transport the gust at the expense of higher computational effort (Heinrich and Reimer, 2013). On the other hand, prescribed velocity methods (field velocity method, FVM (Singh and Baeder, 1997), and split velocity method, SVM (Wales et al., 2014)), define the imposed gust velocity inside the computational domain at each point in space and each instant in time by suitably modifying the governing equations. Such a method is found to be advantageous for many aeronautics applications (e.g., an airfoil penetrating a vertical gust). As shown in Boulbrachene et al. (2021), for horizontally oriented gusts the FVM and the SVM methodologies are not an appropriate choice. Recently, De Nayer and Breuer (2020) proposed a pure source-term (ST) formulation to inject horizontal wind gusts close to the region of interest. Upon injection, the gust is allowed to freely propagate through the domain and, consequently, the full coupling (i.e., including the feedback effect) between the gust and the surrounding field is captured. Therefore, this method is employed in this work.

2.2. Source-term formulation

For simulating fluid–structure interaction problems based on a finite-volume scheme, the Arbitrary Lagrangian–Eulerian (ALE) formulation of the Navier–Stokes equations is applied. Inserting the momentum source-term (ST) formulation for a gust (De Nayer and Breuer, 2020) the integral form of the governing equations describing the fluid flow are written based on the fluid velocity $\tilde{\mathbf{u}}$ as:

$$\frac{d}{dt}\int_{V^{\text{grid}}} \rho \, dV + \int_{S^{\text{grid}}} \rho \, (\tilde{\mathbf{u}} - \mathbf{u}^{\text{grid}}) \cdot \mathbf{n} \, dS = 0 \, ,$$

$$\frac{d}{dt}\int_{V^{\text{grid}}} \rho \, \tilde{\mathbf{u}} \, dV + \int_{S^{\text{grid}}} \rho \, (\tilde{\mathbf{u}} - \mathbf{u}^{\text{grid}}) \tilde{\mathbf{u}} \cdot \mathbf{n} \, dS = \mathbf{S}^{\text{syn}}_{\text{turb}} + \mathbf{S}^{\text{ST}}_{\text{gust}} - \int_{S^{\text{grid}}} \underline{\underline{\tilde{\boldsymbol{\tau}}}} \cdot \mathbf{n} \, dS - \int_{S^{\text{grid}}} p \, \mathbf{n} \, dS \, ,$$

where ρ is the density of the fluid, $\underline{\underline{\tilde{\boldsymbol{\tau}}}}$ is the stress tensor based on the flow velocity $\tilde{\mathbf{u}}$, and $\mathbf{n}$ is the surface normal vector of the considered control volume. Here, the volume and surface integrals are taken over the current time-dependent volume $V^{\text{grid}}(t)$ and the surface $S^{\text{grid}}(t)$ of a grid cell. $\mathbf{u}^{\text{grid}}$ denotes the grid velocity with which the surface of a control volume (CV) is moving. The momentum source term $\mathbf{S}^{\text{syn}}_{\text{turb}}$ describes the synthetically generated turbulent fluctuations to mimic the inflow turbulence as described in Sections 3 and 4. Correspondingly, the momentum source term $\mathbf{S}^{\text{ST}}_{\text{gust}}$ models the contribution of the gust based on the *total* velocity $\mathbf{u}$ and is formulated on the special local basis $\mathcal{B}_1 = (O, \mathbf{g}_1, \mathbf{g}_2, \mathbf{g}_3)$ (see Fig. 1) as follows:

$$\mathbf{S}^{\text{ST}}_{\text{gust}}\big|_{\mathcal{B}_1} = \int_{V^{\text{grid}}} \left(\mathbf{u}|_{\mathcal{B}_1} \cdot \nabla\right) \left(\rho \ \mathbf{u}|_{\mathcal{B}_1}\right) dV \, .$$

The *total* velocity vector $\mathbf{u}$ reads:

$$\mathbf{u} = \tilde{\mathbf{u}} + \mathbf{u}_{\text{g}} \, ,$$

where $\tilde{\mathbf{u}}$ is the flow velocity and the primary variable solved for during the simulation. $\mathbf{u}_{\text{g}}$ describes the imposed analytical gust velocity in the context of deterministic gust models defined as:

$$\mathbf{u}_{\text{g}}\big|_{\mathcal{B}_1}(t, \xi, \eta, \zeta) = A_{\text{g}} \, f_{\text{t}}(t) \, f_1(\xi) \, f_2(\eta) \, f_3(\zeta) \, \mathbf{g_1} \, .$$

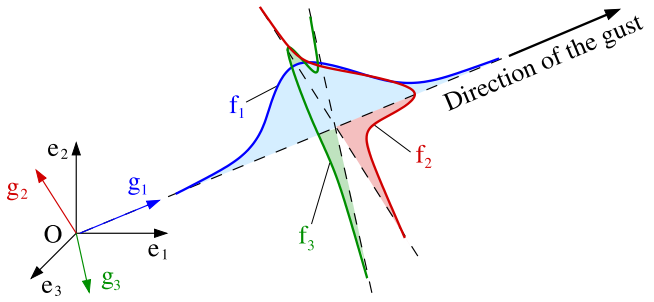

Fig. 1. Definition of the gust in the local basis $\mathcal{B}_1 = (O, \mathbf{g}_1, \mathbf{g}_2, \mathbf{g}_3)$.

The constant A_g defines the strength of the gust and the function f_t the temporal evolution of the gust velocity during the injection phase. The functions f_1, f_2 and f_3 denote the spatial distribution of the gust velocity in $\mathbf{g_1}$, $\mathbf{g_2}$ and $\mathbf{g_3}$ direction, respectively.

The source term for describing the gust is simplified by taking into account that the only non-zero gust velocity component is that of the first vector of the local basis $\mathcal{B}_1$ (i.e., $\mathbf{g_1}$), and assuming that the gradient of the flow velocity along this direction is negligible (i.e., $\frac{\partial \tilde{\mathbf{u}}|_{\mathcal{B}_1}}{\partial \xi} \approx 0$) (see De Nayer and Breuer, 2020). Based on the gust shapes employed in this work, a spatial restriction of the source term in hand is necessary to achieve a favorable positive momentum (see Pasquetti and Peres, 2015; De Nayer and Breuer, 2020). Compiling the points mentioned and approximating the volume integral by means of the midpoint rule, the source term written in the Cartesian basis $\mathcal{B}_0 = (O, \mathbf{e_1}, \mathbf{e_2}, \mathbf{e_3})$ reads:

$$\mathbf{S}^{\mathrm{ST}}_{\mathrm{gust}}\big|_{\mathcal{B}_0} \approx \begin{cases} \rho \;\; A_{\mathrm{g}} \;\; f_{\mathrm{t}}(t) \;\; f_2(t_\eta(x_{\mathrm{cc}}, y_{\mathrm{cc}}, z_{\mathrm{cc}})) \;\; f_3(t_\zeta(x_{\mathrm{cc}}, y_{\mathrm{cc}}, z_{\mathrm{cc}})) \;\; \left.\dfrac{\partial f_1}{\partial \xi}\right|_{\mathrm{cc}} \;\; V^{\mathrm{grid}} \;\; \mathbf{u}_{\mathrm{g}}\big|_{\mathcal{B}_0,\mathrm{cc}} & \text{for} \quad \xi < \xi_g \\ 0 & \text{else} \,. \end{cases} \tag{1}$$

Thus, a distinction is made between the so-called expulsion phase ($\xi < \xi_g$) and the ingestion phase ($\xi > \xi_g$). Here the subscript *cc* is an abbreviation for *cell center*. The functions t_ξ, t_η and t_ζ find the local coordinates ξ, η and ζ based on given Cartesian coordinates, respectively. Finally, the vector $\mathbf{u}_{\mathrm{g}}\big|_{\mathcal{B}_0}$ is expressed as:

$$\mathbf{u}_{\mathrm{g}}\big|_{\mathcal{B}_0}(t, x, y, z) = A_{\mathrm{g}} \;\; f_{\mathrm{t}}(t) \;\; f_1(t_\xi(x, y, z)) \;\; f_2(t_\eta(x, y, z)) \;\; f_3(t_\zeta(x, y, z)) \;\; \mathbf{n}^{\mathrm{g}}\big|_{\mathcal{B}_0} \,, \tag{2}$$

where $\mathbf{n}^{\mathrm{g}}|_{\mathcal{B}_0}$ is the user-defined unit vector defining the direction of the gust in the Cartesian basis.

2.3. Gust shapes

In the following, the spatial functions (f_1, f_2 and f_3) as well as the temporal function f_t characterizing the deterministic gust imposed in the cases presented below are described. For the sake of generality, we let the variable ϕ be equal to the coordinate $\phi = \{x, y, z\}$ or the time t and the subscript i equal to 1, 2, 3 or t, respectively. The constant ϕ_{g} is the central value of the gust distribution for the corresponding ϕ and L^ϕ_{g} its length scale.

- **Adapted "1-cosine" shape** (Extreme Coherent Gust, ECG):
  The original "1-cosine" shape found in the literature can be adapted by introducing the central value ϕ_{g}. That allows to achieve more control than for the original shape:

$$f_{\mathrm{i}}(\phi) = \begin{cases} \dfrac{1}{2}\left(1 + \cos\left(\dfrac{2\pi\,(\phi - \phi_{\mathrm{g}})}{L^\phi_{\mathrm{g}}}\right)\right) & \text{for} \quad (\phi - \phi_{\mathrm{g}}) \in \left[-\frac{L^\phi_{\mathrm{g}}}{2}, \frac{L^\phi_{\mathrm{g}}}{2}\right] \\ 0 & \text{else} \,. \end{cases}$$

In the definition of $\mathbf{S}^{\mathrm{ST}}_{\mathrm{gust}}\big|_{\mathcal{B}_0}$ given by Eq. (1), the first derivative $\partial f_1/\partial \xi$ appears during the expulsion phase, i.e., for $(\phi - \phi_g) \in \left[-\frac{L^\phi_{\mathrm{g}}}{2}, 0\right]$, whereas the source term is forced to zero during the ingestion phase, i.e., for $(\phi - \phi_g) \in \left[0, \frac{L^\phi_{\mathrm{g}}}{2}\right]$. For further details refer to De Nayer and Breuer (2020). In order to guarantee a smooth continuous source term between the expulsion and the ingestion phase at $\phi = \phi_{\mathrm{g}}$, the ECG shape is slightly adapted to deliver a C^2-continuous function for the applied source-term formulation (see the zoomed view in Fig. 2(b)) as follows:

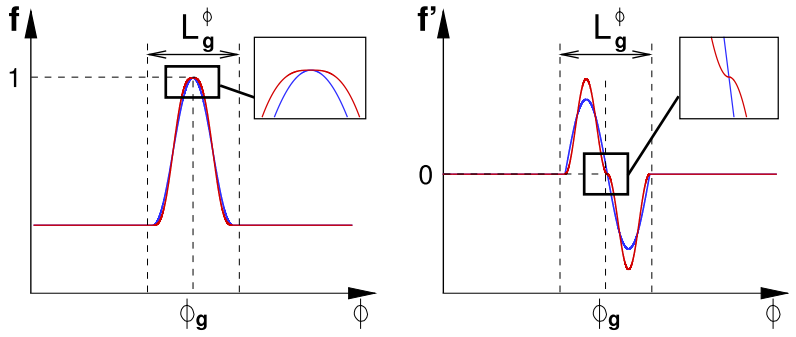

(a) ECG (blue) vs. ECG-C^2 (red). (b) Associated derivatives.

Fig. 2. Adapted "1-cosine" vs. modified C^2-"1-cosine" shapes and their derivatives for a given scale L_g^ϕ and central value ϕ_g.

- **Modified C^2-"1-cosine" shape** (Extreme Coherent Gust C^2, ECG-C^2):

$$f_i(\phi) = \begin{cases} \frac{2}{L_g^\phi}\left(\phi - \left(\phi_g - \frac{L_g^\phi}{2}\right) + \frac{L_g^\phi}{4\pi}\sin\left(\frac{4\pi\left(\phi-\phi_g\right)}{L_g^\phi} + \pi\right)\right) \\ \qquad\qquad \text{for} \quad \left(\phi - \left(\phi_g - \frac{L_g^\phi}{4}\right)\right) \in \left[-\frac{L_g^\phi}{4}, \frac{L_g^\phi}{4}\right] \\ -\frac{2}{L_g^\phi}\left(\phi - \left(\phi_g + \frac{L_g^\phi}{2}\right) + \frac{L_g^\phi}{4\pi}\sin\left(\frac{4\pi\left(\phi-\phi_g\right)}{L_g^\phi} - \pi\right)\right) \\ \qquad\qquad \text{for} \quad \left(\phi - \left(\phi_g + \frac{L_g^\phi}{4}\right)\right) \in \left[-\frac{L_g^\phi}{4}, \frac{L_g^\phi}{4}\right] \\ 0 \qquad\qquad\qquad\qquad\qquad\qquad \text{else} \ . \end{cases}$$

Fig. 2 illustrates both distributions for a given scale L_g^ϕ and a central value ϕ_g.

The duration of the gust L_g^t is linked to the spatial length scale of the gust in streamwise direction L_g^ξ by the expression:

$$L_g^\xi = L_g^t \ u_g^{\text{conv}} \ ,$$

where u_g^{conv} is an approximation of the convective velocity of the wind gust in the surrounding flow field. In the following, the default value is the free-stream velocity $u_g^{\text{conv}} = u_\infty$.

3. Simulation framework for CFD and FSI problems within turbulent flows

In order to solve pure CFD problems, the 3D fully parallelized finite-volume fluid solver FASTEST-3D is applied (Durst and Schäfer, 1996). Since modern realistic test cases imply turbulent flows, FASTEST-3D includes different techniques to predict this kind of flows. In the present study the large-eddy simulation (LES) technique is used, i.e., the large scales of the turbulent flow field are resolved directly, whereas the non-resolvable small scales have to be taken into account by a subgrid-scale (SGS) model. The classical Smagorinsky (1963) SGS model applying the standard parameter $C_s = 0.1$ combined with the Van-Driest damping function is used, since preliminary work in De Nayer et al. (2018b) shows that for the test case considered the model delivers reasonable results.

Since LES is applied, a semi-implicit predictor–corrector scheme (projection method) of second-order accuracy in space and time is preferred over the standard implicit SIMPLE scheme for the solution of the pressure–velocity coupling problem (Breuer et al., 2012). The filtered Navier–Stokes equations are discretized on a curvilinear, block-structured body-fitted grid with a collocated variable arrangement. Standard discretization methods such as mid-point rule and blended central scheme (5% upwind) are set as in Wood et al. (2016).

In order to mimic a realistic turbulent inflow, synthetic turbulent perturbations are injected into the computational domain upstream of the zone of interest (here the hemispherical structure). These synthetic data are generated using the so-called Synthetic Turbulent Inflow Generator (STIG) relying on the digital filter concept of Klein et al. (2003) and introduced into the domain based on the source-term method by Schmidt and Breuer (2017), Breuer (2018) and De Nayer et al. (2018b).

Facing an FSI problem, the simulation framework has to be extended. Based on a partitioned procedure detailed in Breuer et al. (2012), the fluid solver FASTEST-3D is coupled with the computational structure dynamics (CSD) solver Carat++ (Bletzinger et al., 2006). The coupling and the mapping between the two diverse surface discretizations at the FSI

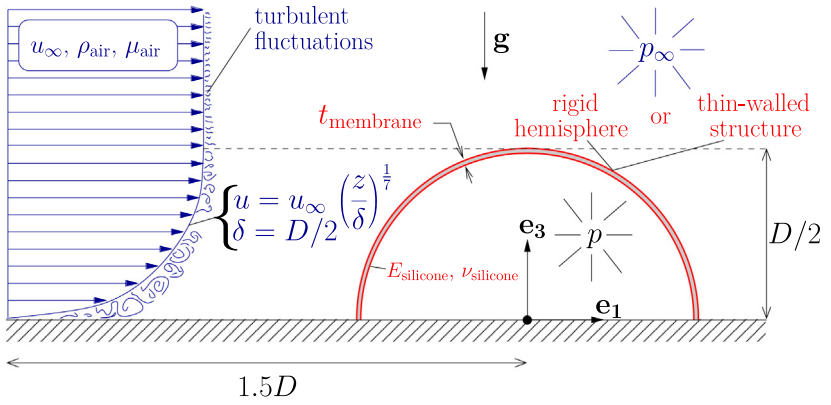

Fig. 3. Surface-mounted rigid (see Section 4) or air-inflated flexible hemisphere (see Section 5) within a turbulent boundary layer.

interface are carried out by the open-source software EMPIRE (Sicklinger et al., 2014). Validation cases can be found in De Nayer et al. (2014) and De Nayer and Breuer (2014).

Since the FSI simulation framework relies on body-fitted meshes, FASTEST-3D is written in the ALE formulation given in Section 2. To describe the fluid motion in temporally varying domains, the fluid mesh has to be adapted at each time step. Different techniques are available: In case of small deformations a very fast algebraic procedure is performed based on a combination of linear and transfinite interpolations (TFI) (Thompson et al., 1985). If the deformations become significant, a hybrid adaption method especially developed for FSI problems within LES (Sen et al., 2017) is applied. It relies on a combination of an inverse distance weighting interpolation for the block boundaries of the block-structured grid and a three-dimensional TFI for the inner mesh.

The deformation of the structure due to the fluid loads at the FSI interface is predicted by Carat++. It is a finite-element and an isogeometric solver for the structure developed with emphasis on the prediction of the mechanical behavior of thin-walled structures (i.e., shells and membranes). Furthermore, structural optimization and form finding procedures for pre-stressed tensile structures are available in the software (Breitenberger et al., 2015; Philipp et al., 2016). The momentum equation written in a Lagrangian frame of reference is applied to describe the dynamic equilibrium of the structure. A St. Venant–Kirchhoff material law is assumed and links the Piola–Kirchhoff stress tensor with the Green–Lagrange strain tensor (Basar and Weichert, 2013).

EMPIRE (*Enhanced Multi Physics Interface Research Engine*) is an open-source coupling tool dedicated to co-simulations with n clients ($n \geq 2$). This library allows the user to generate its own coupling algorithms by writing a user-defined xml input file. Standard coupling algorithms such as loose or strong staggered schemes or more complex approaches such as Jacobian-based schemes can be easily defined. EMPIRE does the mapping between the non-matching CFD and CSD grids and the exchange of data with its clients. Details about the presently applied mortar mapping in case of FEM or IGA discretizations can be found in Wang et al. (2016) or Apostolatos et al. (2019b).

4. Rigid hemisphere within a turbulent boundary layer

4.1. Description of the CFD case

The investigated hemispherical rigid body (diameter D) is mounted on an uniform smooth wall as depicted in Fig. 3. The origin of the frame of reference is taken at the center of the base area of the hemisphere, where $x = \mathbf{e_1}$ denotes the streamwise, $y = \mathbf{e_2}$ the spanwise and $z = \mathbf{e_3}$ the vertical (wall-normal) direction. The structure is put into a thick turbulent boundary layer, where the distribution of the time-averaged velocity in main flow direction closely follows the 1/7 power law. At a distance of 1.5 diameters upstream of the bluff body the thickness of the boundary layer δ corresponds to the height of the hemisphere ($\delta = D/2$) (see Wood et al., 2016).

Contrary to the case presented in Wood et al. (2016) the Reynolds number of the air flow ($\rho = \rho_{air} = 1.225$ kg/m^3, $\mu_{air} = 18.27 \times 10^{-6}$ kg/(m s) at $\vartheta = 20°$ C) is set to Re = $\rho_{air}\, D\, u_\infty / \mu_{air} = 100{,}000$ and corresponds to one of the cases of Wood et al. (2018). u_∞ is the undisturbed free-stream mean velocity in x-direction at standard atmospheric conditions. The Mach number is low (Ma ≤ 0.03). The air flow can be assumed to be incompressible and isotherm. The results will be given in dimensionless form based on D, u_∞ and ρ_{air}.

4.2. Computational setup

To simulate the flow, the chosen computational domain is a large hemispherical expansion (radius $10\,D$) with its origin at the center of the hemisphere. A medium block-structured mesh is used composed of 4.3×10^6 control volumes.

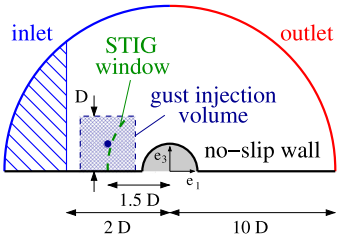

(a) 2D sketch with boundary conditions.

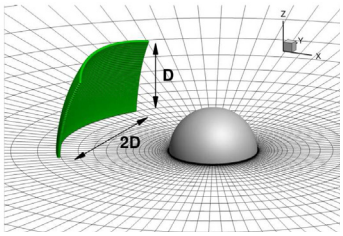

(b) STIG injection window (Only every fifth line of the bottom grid is displayed).

Fig. 4. Boundary conditions, STIG injection window and gust injection window used for the simulation.

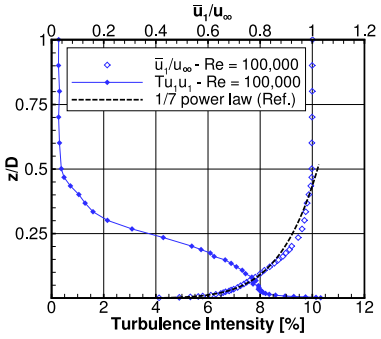

(a) Streamwise mean velocity and turbulence intensity.

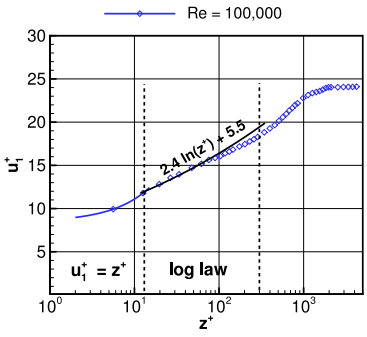

(b) u^+ (z^+) distribution.

Fig. 5. Velocity and turbulence intensity in streamwise direction for the turbulent boundary layer at Re = 100,000. Measured by Wood et al. (2018) at $-1.5\,D$ in front of the hemisphere.

Comparisons with a fine mesh were carried out in De Nayer et al. (2018b). The viscous sublayer is fully resolved and the first cell center is approximately located at a distance of $\Delta z/D \approx 5 \times 10^{-5}$ from the wall. The aspect ratio of the cells on the hemispherical body is in the range between 1 and 10. The geometric stretching ratios are kept below 1.1. Based on these parameters the dimensionless cell sizes in the wall-normal and tangential directions still fit to the recommendations by Piomelli and Chasnov (1996) for wall-resolved LES. The time step is chosen equal to $\Delta t^* = \Delta t\, u_\infty / D = 3.317 \times 10^{-5}$.

Since the predictions are wall-resolved, the bottom of the domain and the surface of the hemisphere are no-slip walls. The outer surface of the hemispherical expansion is divided into inlet and outlet patches (see Fig. 4). At the outlet a combination of a convective boundary condition and a zero velocity-gradient boundary is applied. The latter is used in those regions which are not strongly influenced by vortical flow structures. The convective velocity is set according to the 1/7 power law.

In order to prescribe a realistic turbulent inflow ignoring the wind gust at the moment, synthetic perturbations are injected into the computational domain upstream of the rigid body. For the generation of the synthetic inflow data the time-averaged velocities and Reynolds stresses measured in the experiment (see Fig. 5 and Wood et al., 2018) are taken. Since it was not possible to determine all Reynolds stress components in the direct vicinity of the wall, these measurements have been complemented by DNS data of Schlatter et al. (2009).

The other important parameters to be defined are the integral time and length scales. The digital filter concept of Klein et al. (2003) solely allows to define a constant value within the entire boundary layer. Thus, a reasonable compromise is required. In the present case, only the turbulent structures injected at $z/D < 0.5$ ($z^+ < 1140$) will have an impact on the bluff body and therefore will mainly drive the flow around the hemisphere. Moreover, looking at the distribution of the turbulence intensity, the most intensive structures are at $z/D \lesssim 0.3$ ($z^+ \lesssim 680$). The dominant structures present in a turbulent boundary layer are the streaks and the hairpin vortices. Since the streaks are confined near the wall in the buffer layer, it was decided to generate synthetic turbulent structures of the size of typical hairpin vortices. These structures have a characteristic streamwise dimension of $\Delta x^+ = 200$ (Bailly and Comte-Bellot, 2015) or 300 (Lesieur, 2008) near the wall and of $\Delta x^+ = 140$ in the logarithmic region, a spanwise extension of about $\Delta y^+ = 100$ and a height between $\Delta z^+ = 200$ and 400 (Adrian, 2007).

The STIG injection window is located approximately $-1.5\,D$ upstream of the body (see Fig. 4). It has an height of approximately $1\,D$ and a width of $2\,D$. Based on the grid resolution of the STIG injection window ($-1 \leq y/D \leq 1$ with

$\Delta y^{\mathrm{STIG}}/D = 1.021 \times 10^{-2}$ and $0 \leq z/D \leq 1$ with $\Delta z^{\mathrm{STIG}}/D = 2.191 \times 10^{-3}$) and the fact that the support of the filters as defined in Klein et al. (2003) should be at least 2, i.e., $n_y = L_y^{\mathrm{STIG}}/\Delta y^{\mathrm{STIG}} = 2$, it leads to a minimum length scale $L_y^{\mathrm{STIG}}/D = 2.04 \times 10^{-2}$. Since the integral length scales are assumed to be equal in all directions, the integral length scale in wall-normal direction is $L_z^{\mathrm{STIG}}/D = L_y^{\mathrm{STIG}}/D = L^{\mathrm{STIG}}/D = 2.04 \times 10^{-2}$. Using the classical length scale specification for the log-law region $L = \kappa\ z$ applied in the mixing length concept by Prandtl, the height where this integral length scale is reached is equal to $z^+ = 165$ with $u_\tau = 0.374$ m/s at Re = 100,000. The dimensionless integral time scale is deduced with the help of the Taylor hypothesis and set to $T^{\mathrm{STIG}}\, u_\infty/D = L^{\mathrm{STIG}}\, u_\infty/(D\, u_1(z^+ = 165)) = 2.85 \times 10^{-2}$. With this value the STIG produces synthetic turbulent structures with a dimensionless size of about $\Delta x^+ = \Delta y^+ = \Delta z^+ = 4\, L^{\mathrm{STIG}}\, \rho_{\mathrm{air}}\, u_\tau/\mu_{\mathrm{air}} \approx 300$ in each direction[1]. This is a good compromise between the size of typical hairpin structures in streamwise, spanwise and wall-normal direction.

For the STIG-R injection method (see De Nayer et al., 2018b), the 3D influence area is defined by a Gaussian distribution. In the present setup, the integral length scale in streamwise direction L^{STIG} is rather small and shorter than the cell size of the injection plane located approximately $-1.5\, D$ upstream of the body. Therefore, the source term has to be scaled according to the second scenario given in De Nayer et al. (2018b). In the present case the influence area is $L_{\mathrm{inf}}/D = 2\, L^{\mathrm{STIG}}/D = 4.08 \times 10^{-2}$ and thus smaller than $\Delta d_0/D = 8. \times 10^{-2}$, where Δd_0 is the width of the grid cell corresponding to the injection patch. It leads to $S_\phi^{\mathrm{CFD}}(x_i) = \sqrt{2}\, \mathrm{erf}(\sqrt{\pi/2})\, \dfrac{L^{\mathrm{STIG}}}{\Delta d_0}\, S_\phi^{\mathrm{syn}}$.

A total of 480,000 time steps of synthetic turbulent inflow data corresponding to about 15 dimensionless time units are generated.

5. Air-inflated flexible hemisphere within a turbulent boundary layer

5.1. Description of the FSI case

The rigid hemisphere used in the above case is now replaced by a thin-walled membranous structure pressurized on the inside by air in a form of a hemisphere as shown in Fig. 3. As before it is mounted on a smooth flat plate and plunged into the same turbulent boundary layer as for the rigid case (see Section 4.1 and Wood et al. (2018) for details). Additionally, the setup is now exposed to the gravitational acceleration $\mathbf{g} = -9.81\ \mathbf{e_3}$.

In the experimental setup of Wood et al. (2018) the thin membrane is made of silicone (Wacker Elastosil 625). To model this material using the St. Venant–Kirchhoff assumption, its density, Young's modulus and Poisson's ratio were experimentally determined in Wood et al. (2018) to $\rho_{\mathrm{silicone}} = 1050\,\mathrm{kg/m^3}$, $E_{\mathrm{silicone}} = 7 \times 10^5$ Pa and $\nu_{\mathrm{silicone}} \approx 0.45$, respectively. More details about these material assumptions can be found in De Nayer et al. (2018a). The thickness of the membrane t_{membrane} is not exactly constant along the structure ($t_{\mathrm{membrane}} \in \left[1.2 \times 10^{-4}\,\mathrm{m}, 2 \times 10^{-4}\,\mathrm{m}\right]$). Preliminary predictions made on pure structural test cases show that an average thickness of $t_{\mathrm{membrane}} = 1.65 \times 10^{-4}$ m delivers good agreement with the experiments (De Nayer et al., 2018a).

One important parameter has also to be set: The pressure difference between the inner gauge pressure of the structure and the pressure outside $\Delta p_{\mathrm{FSI}} = p - p_\infty$. In order to set a sufficiently high inner pressure to stabilize the structure, but also not a too strong gauge pressure to match the desired shape of the hemisphere, a value of $\Delta p_{\mathrm{FSI}} = 43$ Pa is chosen through the calibration process described in Wood et al. (2018).

5.2. Computational FSI setup

Based on the FSI simulation framework described in Section 3, the computational setup for the current test case is as follows. The setup for the fluid part is exactly the same as for the rigid case detailed in Section 4.2. The CSD computational setup relies on the preliminary works of De Nayer et al. (2018a) and Apostolatos et al. (2019b). Two different kinds of simulations will be presented and compared in the result part:

- The first is based on the FEM discretization of the thin-walled structure with a grid containing 1926 *Constant Strain Triangle* (CST) elements and 999 nodes. All nodes have three degrees of freedom except the ones connected with the smooth plate at $z/D = 0$. These nodes cannot move in any translational direction. Mesh studies can be found in De Nayer et al. (2018a).
- The second relies on the IGA discretization of the membrane by a single patch containing 625 bi-quadratic C^1-continuous elements. The hemispherical shape is attained by a form-finding analysis. Details of preceding investigations and visualizations of the mesh can be found in Apostolatos et al. (2019b).

The static pressure difference Δp_{FSI} is considered constant during the simulation and is modeled in the CSD solver by a follower pressure load acting on each surface element. With this simplification the air flow in the inner domain has not to be solved by the fluid solver. Additionally, the gravitational acceleration is taken into account in the CSD solver as a dead load acting on the volume of each element. Moreover, an initial homogeneous and isotropic pre-stress

[1] For more details, we refer to De Nayer et al. (2018a).

Table 1
Gusts characteristics for ST formulation.

gust	$\mathbf{g}_1$	A_g	$f_t(t) = \text{ECG-}C^2$	$f_1(\xi) = \text{ECG-}C^2$	$f_2(\eta) = \text{ECG}$	$f_3(\zeta) = \text{ECG}$
			L_g^t	L_g^ξ	L_g^η	L_g^ζ
weak	$\mathbf{e}_1$	$0.5\,u_\infty$	$L_g^\xi/u_g^{\text{conv}}$	$1\,D$	$1\,D$	$1\,D$
medium	$\mathbf{e}_1$	u_∞	$L_g^\xi/u_g^{\text{conv}}$	$1\,D$	$1\,D$	$1\,D$
strong	$\mathbf{e}_1$	$1.5\,u_\infty$	$L_g^\xi/u_g^{\text{conv}}$	$1\,D$	$1\,D$	$1\,D$

tensor field $\mathbf{n}_0$ is applied as usual with membrane elements. A previous investigation (De Nayer et al., 2018a) based on the experimental steady calibration case of Wood et al. (2018) delivered a value of $n_{\text{membrane}} = 7794.5$ Pa. The standard second-order non-linear Newmark scheme is applied with the same dimensionless time step as the fluid solver, i.e., $\Delta t^* = \Delta t\, U_\infty / D = 3.317 \times 10^{-5}$. In addition, the structural damping of the hemisphere has to be taken into account, since the material is silicone. A Rayleigh damping with the mass- and stiffness-proportional parameters set to $\alpha_r = 17.47$ and $\beta_r = 1.89 \times 10^{-4}$, is applied (De Nayer et al., 2018a).

Concerning the FSI coupling between fluid and structure parts, a loose coupling scheme is preferred to minimize the data exchange and the mesh adaption, since the ratio of the structural density to the fluid density is large ($\rho_{\text{silicone}}/\rho_{\text{air}} \approx 857$).

6. Wind gust settings

For a practical application of wind gusts hitting rigid and flexible structures as investigated in the present study, the gusts are directed parallel to the streamwise direction. An appropriate gust injection region is selected in the upstream area of the structure in such a way that it is not too close in order to give the gust a room to develop. At the same time it should be not too far in order to avoid numerical dissipation and long simulation times. Therefore, the center of the gust at the beginning of the ST injection is located at the point $(-1.5\,D, 0, D/2)$. Based on the definition of the gust introduced in Section 2, the vector $\mathbf{n}^g|_{\mathcal{B}_0}$ defining the gust direction in the Cartesian basis $\mathcal{B}_0$ is equal to the basis vector $\mathbf{e}_1$, which represents the streamwise direction. Consequently, the vector $\mathbf{g}_1$ of the local gust basis is identical to $\mathbf{e}_1$. The gust velocity component given by Eq. (2) is defined as follows:

The temporal shape function $f_t(t)$ follows the same analytical function as the spatial shape $f_1(\xi)$ oriented in streamwise direction in the present case. The special ECG-C^2 shape is selected for both. In the spanwise and vertical directions (i.e., $\mathbf{g}_2 = \mathbf{e}_2$ and $\mathbf{g}_3 = \mathbf{e}_3$, respectively), a standard ECG shape is selected, i.e., $f_2(\eta) = f_3(\zeta) = \text{ECG}$.

The parameters to be defined next are the temporal and spatial scales in each direction. Since the temporal scale is deduced from the spatial length scale in the streamwise direction with $L_g^t = L_g^\xi/u_g^{\text{conv}}$, only three spatial scales are required (i.e., L_g^ξ, L_g^η and L_g^ζ). In this study, these length scales are chosen in such a way that the body of the wind gust can completely cover the whole structure. Since the body has a length and a width of $1\,D$, the gust length scales along the streamwise and the spanwise directions (i.e., L_g^ξ and L_g^η) are set to $1\,D$. It is also worth mentioning that a streamwise gust length scale of $1\,D$ is sufficient since it is much longer than the largest vortical structures injected by the synthetic turbulent generator (see Section 4.2). Similarly, given that the height of the rigid hemisphere is $D/2$, the half of the gust length scale along the vertical direction is set to a value of $D/2$ (or $L_g^\zeta = 1\,D$). Here, three gust strengths are investigated, a *weak* gust with an amplitude A_g of $u_\infty/2$, a *medium* gust with an amplitude of u_∞ and a *strong* gust with $A_g = 1.5\,u_\infty$. The gust characteristics of the simulations performed for the rigid and flexible cases are summarized in Table 1.

7. Results and discussion

7.1. Propagation of the gusts upstream of the rigid or flexible hemisphere

Fig. 6 compares the temporal evolution of the dimensionless streamwise velocity u_1/u_∞ and the dimensionless pressure $p/(\rho_{\text{air}}\, u_\infty^2)$ for three different wind gusts injected by the ST method. The case without gust is plotted as a reference and the fluctuations observed in this case are due to the incoming turbulent flow. The four selected monitoring points are located upstream of the rigid or flexible body and their positions are at the height of the gust center $(z/D = 0.5)$ in the symmetry plane $(y/D = 0)$ (see Fig. 7(d)). The temporal evolutions in the approaching phase of the gusts are displayed in Fig. 6 as a function of the dimensionless time $t^* = t\, u_\infty / D$. $t^* = 0$ corresponds to the beginning of the gust injection, whereas $t^* = 1$ defines the end of the injection. The gusts differ in terms of their amplitudes A_g. As expected, the stronger the amplitude of the gust is, the stronger is the maximum of the total velocity obtained, where the latter can be roughly estimated by $u_1^{\max}/u_\infty = 1 + A_g/u_\infty$. Furthermore, the asymmetry in the obtained temporal gust histories increases with rising gust amplitudes A_g. The variation of the pressure at the location of the gust is as follows. In the phase, when the fluid velocity increases for example at point P01 or P02, the pressure is higher than without the gust. However, when the center of the gust has already passed a certain location and the fluid velocity decreases again, the pressure level is smaller than without the gust and then returns to atmospheric pressure. Obviously, the stronger the gust

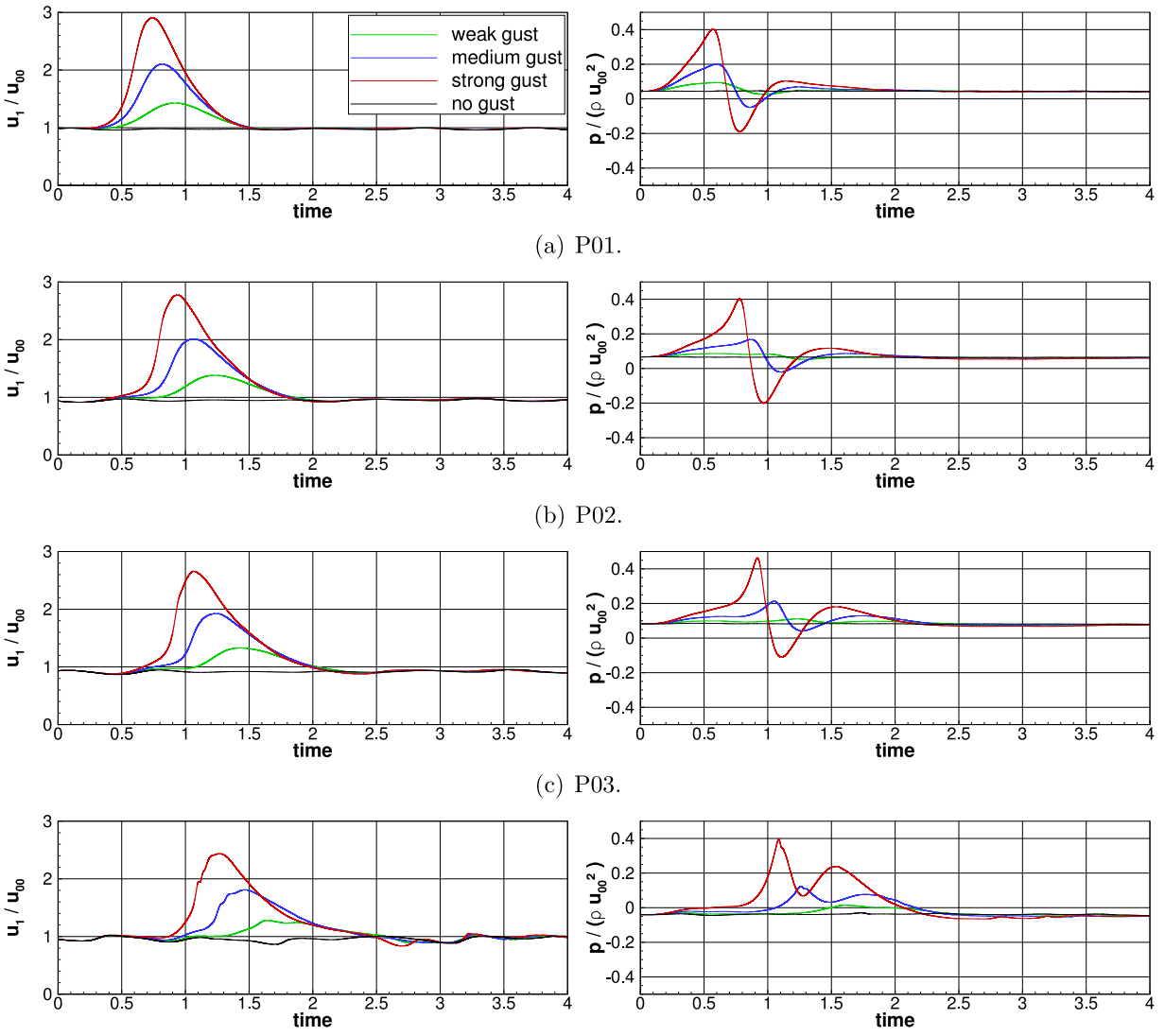

Fig. 6. Comparison of wind gusts with varying amplitudes upstream of the rigid body at four monitoring points ($L_g^{\xi} = 1D$, $L_g^{\eta} = 1D$, $L_g^{\zeta} = 1D$, $u_g^{\text{conv}} = u_\infty$). *Left:* Streamwise velocity; *Right:* Pressure.

is, the stronger is the rise and fall of the pressure, where a quadratic relationship between the pressure changes and the gust amplitude has to be expected.

Figs. 7(a) to 7(c) depict the *medium* gust approaching the rigid hemisphere under three different views at $t^* \approx 0.95$. This instant in time is just before the impact of the gust on the body. Since the gust is defined as a short but strong variation of the velocity, the streamwise velocity u_1/u_∞ is chosen for the visualization. Additionally, the gust structure itself is highlighted by the red iso-surface with $u_1/u_\infty = 1.4$. For a direct comparison with the predicted flow field without a wind gust using the same turbulent inflow data, Figs. 7(d) to 7(f) depict the corresponding data for exactly the same views and the same instant in time. This contrasting juxtaposition shows very clearly that the flow field around the hemisphere and in its wake is not at all influenced by the wind gust at this point in time. Solely in front of the bluff body the effect of the gust can apparently be seen in form of an increased level of the wind speed in the main flow direction. Similar to the streamwise velocity the pressure distribution around the hemisphere and in its wake is not affected by the gust (see Fig. 8). Upstream of the body the increase of the velocity due to the presence of the gust leads to a local decrease of the pressure at the position of the gust.

At approximately $t^* \approx 1$ the gust hits the body. The effects of this impact on the forces, the gust structure and later on the deformations are discussed in the subsequent sections.

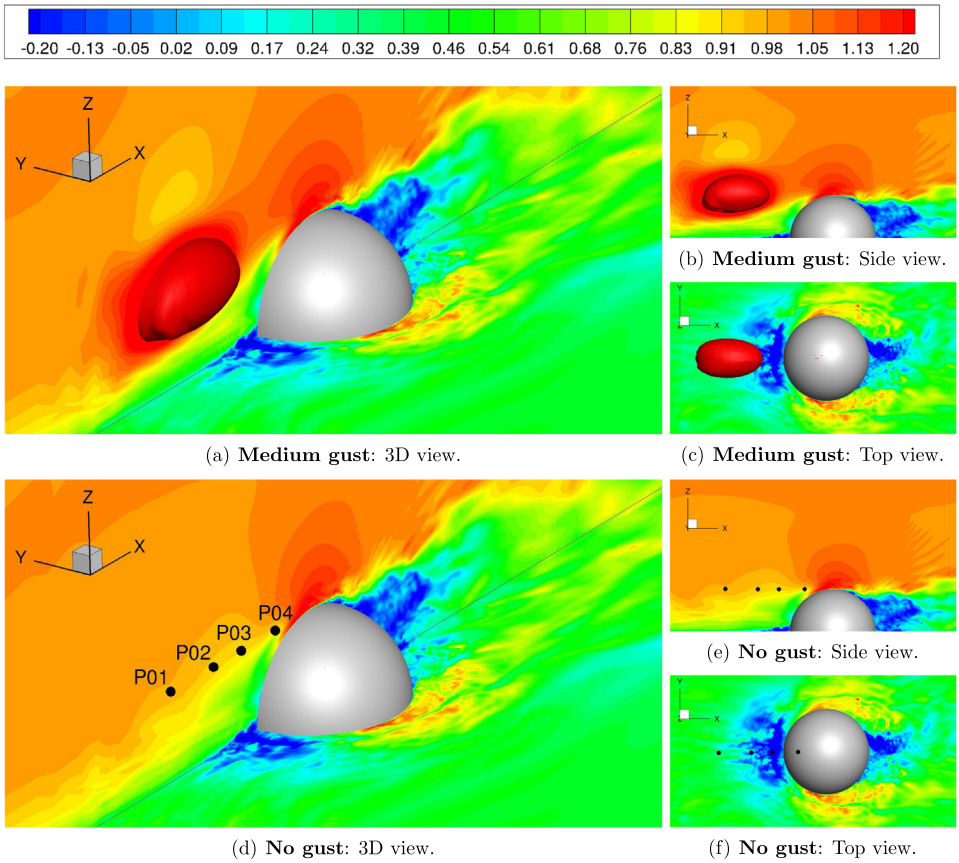

(a) **Medium gust**: 3D view.

(b) **Medium gust**: Side view.

(c) **Medium gust**: Top view.

(d) **No gust**: 3D view.

(e) **No gust**: Side view.

(f) **No gust**: Top view.

Fig. 7. Instantaneous snapshot of the *medium* gust approaching the rigid hemisphere at $t^* \approx 0.95$ (top: (a)–(c)) compared with the same snapshot without gust (bottom: (d)–(f)). Streamwise velocity u_1/u_∞ in a slice near the bottom wall and in the symmetry plane $y = 0$. The gust structure is highlighted by an iso-surface of the streamwise velocity $u_1/u_\infty = 1.4$.

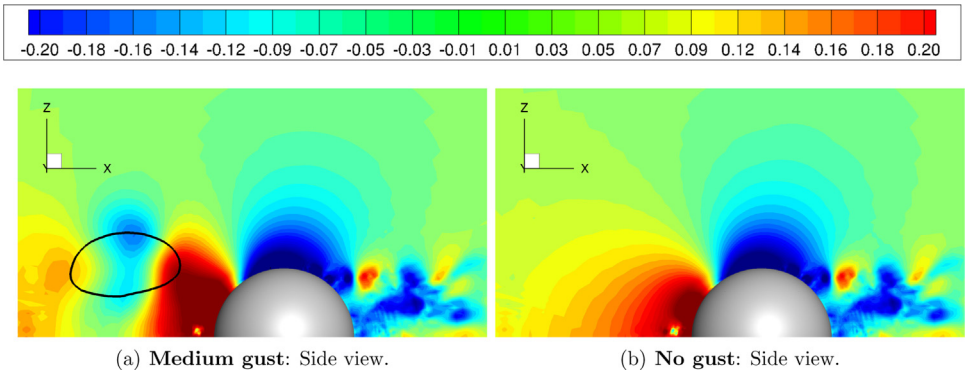

(a) **Medium gust**: Side view.

(b) **No gust**: Side view.

Fig. 8. Instantaneous snapshot of the *medium* gust approaching the rigid hemisphere at $t^* \approx 0.95$ (a) compared with the same snapshot without gust (b). Pressure $p/(\rho_{\text{air}} u_\infty^2)$ in the symmetry plane $y = 0$. The gust position is highlighted by a black iso-line of the streamwise velocity $u_1/u_\infty = 1.4$.

7.2. Impact of the gusts on the rigid hemisphere and resulting fluid forces

The entire development of the flow field during the approach and impact of the gust is shown for the case of the *medium* gust strength in Figs. 9 and 10. Again the streamwise velocity in a slice near the bottom wall and in the symmetry plane is displayed in Fig. 9 but now for six instants in time, which describe the entire process of the impact and disappearance of the gust. Furthermore, the gust structure is highlighted again by an iso-surface with $u_1/u_\infty = 1.4$. The pressure distribution is additionally presented in Fig. 10, where the iso-surface tracking of the gust structure is replaced by an

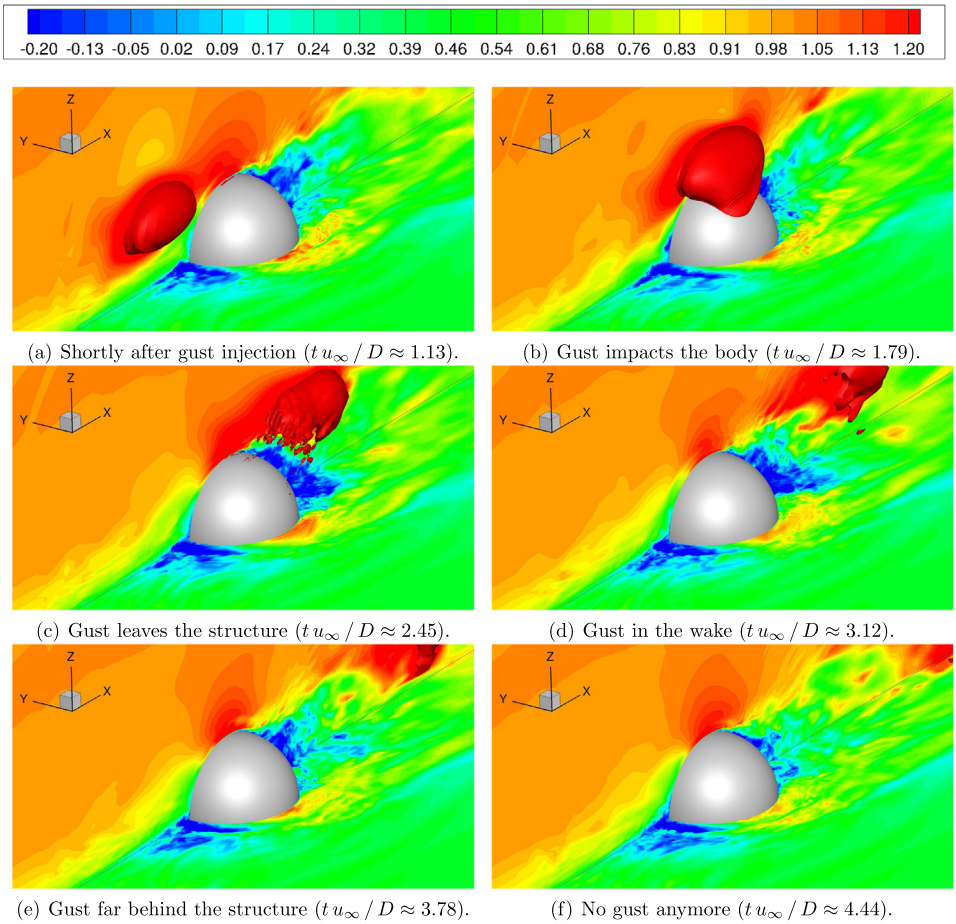

(a) Shortly after gust injection ($t\,u_\infty / D \approx 1.13$).
(b) Gust impacts the body ($t\,u_\infty / D \approx 1.79$).
(c) Gust leaves the structure ($t\,u_\infty / D \approx 2.45$).
(d) Gust in the wake ($t\,u_\infty / D \approx 3.12$).
(e) Gust far behind the structure ($t\,u_\infty / D \approx 3.78$).
(f) No gust anymore ($t\,u_\infty / D \approx 4.44$).

Fig. 9. Rigid case: *Medium* wind gust moving downstream and impacting the rigid hemisphere (streamwise velocity u_1/u_∞ in a slice near the bottom wall and in the symmetry plane $y = 0$). The gust structure is highlighted by an iso-surface of the streamwise velocity $u_1/u_\infty = 1.4$.

iso-line in the symmetry plane to see the pressure changes hidden behind the gust structure. In order to quantify the effect of the gust on the structure, the resulting forces in streamwise and vertical direction are shown in Fig. 11 as a function of the dimensionless time. Note that the forces are also made dimensionless leading to the force coefficients c_x and c_z defined as the forces divided by the stagnation pressure $\rho_{\text{air}}\,u_\infty^2/2$ and the reference area $\pi\,D^2/8$. In addition, the pressure force related parts of the total force coefficients, c_x^p and c_z^p, are plotted. It can be clearly seen in Fig. 11 that the major contribution of the force coefficient for this geometry is the pressure. Especially for the vertical component the shear stresses only marginally contribute to the total force.

After its injection the *medium* wind gust impacts the front of the rigid hemisphere at about $t^* \approx 1.13$ (see Fig. 9(a)) leading to an increase of the streamwise force coefficient c_x (blue curve in Fig. 11(a)). At this first instant in time the fluid load on the hemisphere is only a bit higher than for the case of the turbulent flow without gust. After reaching this first maximum at $t^* \approx 1.2$, c_x decreases, since the high pressure area in front of the body alleviates as the gust approaches the tip of the rigid body. In the next time instant displayed in Fig. 9(b) the gust has moved downstream and hits the tip at about $t^* \approx 1.8$. At this time the vertical force coefficient c_z (blue curve in Fig. 11(b)) reaches a maximum, since the pressure minimum is above the hemisphere (see Fig. 10(b)). Simultaneously the streamwise force coefficient c_x tends towards its global maximum at $t^* \approx 2$, since at that time the pressure minimum is on the back side of the structure (see the low pressure zone moving from the tip to the back in Figs. 10(b) and 10(c)). At the third instant in time (see Fig. 9(c)) the wind gust detaches from the body. The vertical force coefficient c_z reaches its minimum at that time and also c_x decreases since the effect of the pressure minimum gets weaker with increasing distance between the gust and the hemisphere (see the differences in the low pressure area behind the hemisphere in Figs. 10(c) and 10(d)). At $t^* \approx 3.12$ (Fig. 9(d)) the gust is still visible in the wake of the body. The two force components on the structure show a different behavior. The streamwise force coefficient c_x drops to a level, which is below the value of the case without the gust, whereas c_z is still slightly higher than in the case without the gust. The last two instants in time displayed in Figs. 9(e) and 9(f) depict how the gust leaves the region of interest. The zone of low pressure induced by the gust in the vicinity

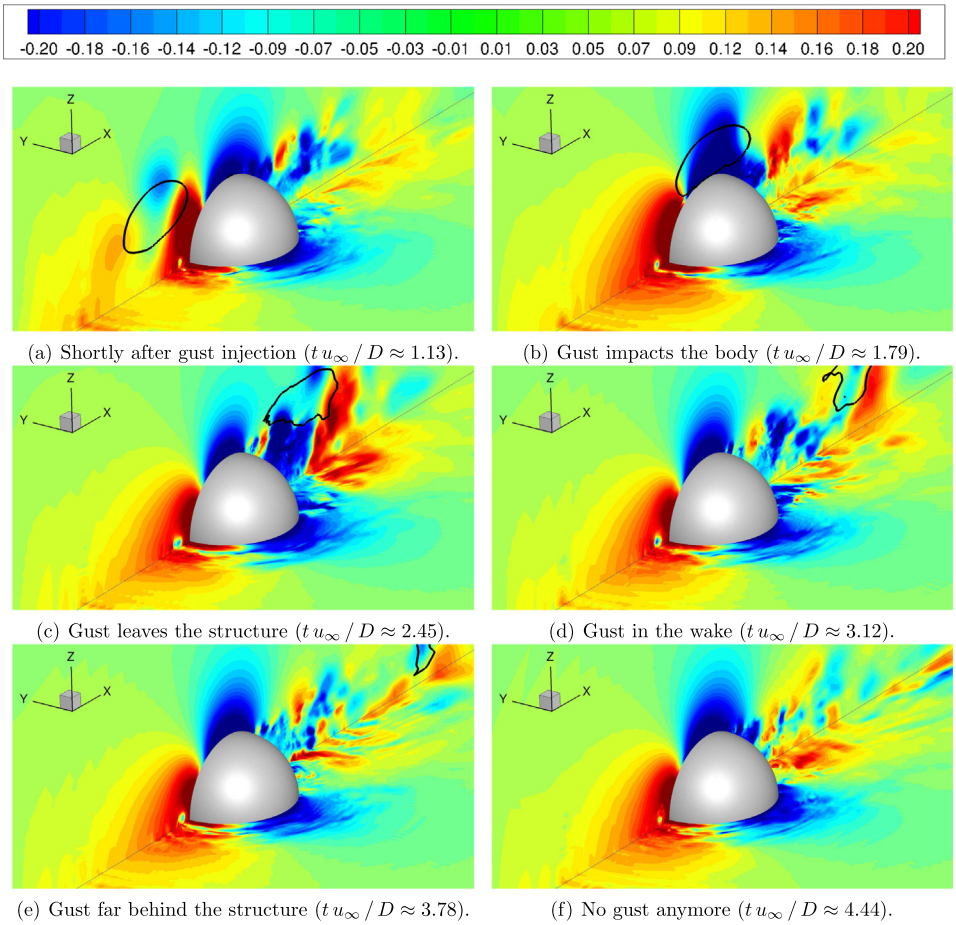

(a) Shortly after gust injection ($t\,u_\infty / D \approx 1.13$). (b) Gust impacts the body ($t\,u_\infty / D \approx 1.79$).

(c) Gust leaves the structure ($t\,u_\infty / D \approx 2.45$). (d) Gust in the wake ($t\,u_\infty / D \approx 3.12$).

(e) Gust far behind the structure ($t\,u_\infty / D \approx 3.78$). (f) No gust anymore ($t\,u_\infty / D \approx 4.44$).

Fig. 10. Rigid case: *Medium* wind gust moving downstream and impacting the rigid hemisphere (pressure $p/(\rho_{\text{air}} u_\infty^2)$ in a slice near the bottom wall and in the symmetry plane $y = 0$). The gust position is highlighted by a black iso-line of the streamwise velocity $u_1/u_\infty = 1.4$ in the symmetry plane.

of the body has vanished (see Figs. 10(e) and 10(f)). Consequently, both force coefficients reach a similar level as for the case without the gust again. Since the wind gust has significantly affected the turbulent flow field around the bluff body, one cannot expect the time histories to converge when the gust has passed the hemisphere.

Fig. 12 gathers the streamwise and vertical force coefficients obtained for different gust strengths. The effects of the *weak* gust on c_x and c_z are minor. Both local maxima of c_x are present, but with low amplitudes and close to each other. Concerning c_z the local maximum is reached at about $t^* \approx 2$ and thus about 0.23 dimensionless time units later than for the *medium* gust discussed before. This observation can be explained by the lower traveling velocity of the *weak* gust compared with the *medium* gust. Similarly, the local maximum of c_z for the *strong* gust is about 0.24 time units earlier than for the *medium* gust.

By increasing the strength of the gust the amplitudes of both local c_x maxima increase. Additionally, the duration between both maxima decreases with intensified gust strength, since the traveling velocity of the gust is higher. As expected, the maximum of c_z augments as well, since the low pressure area at the tip of the hemisphere becomes stronger in case of a more powerful gust. As mentioned before for the *medium* gust, the pressure force is the major contribution to the total force in both streamwise and vertical direction for all gust strengths. Therefore, the peak values of the force coefficients quadratically change with the oncoming velocity, which is given by the superposition of the approaching boundary layer velocity and the velocity of the wind gust.

7.3. Impact of the gusts on the flexible hemisphere and resulting fluid forces and deformations

7.3.1. Detailed analysis for the medium gust

In the following, the setup changes to investigate the FSI case of an air-inflated flexible hemisphere under different wind gust loads. As in the previous section, the global force coefficients c_x and c_z are considered first. Fig. 13 compares the

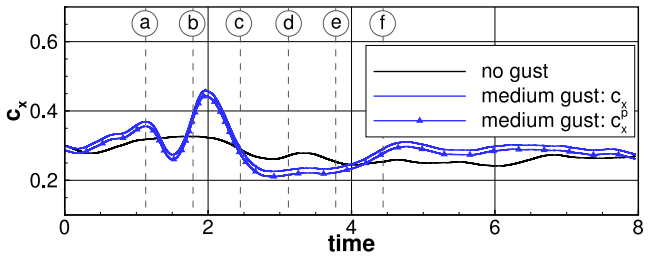

(a) Force coefficient c_x.

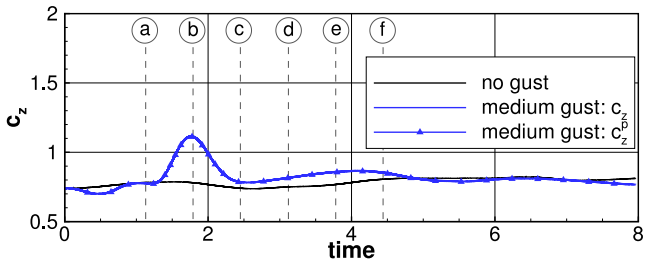

(b) Force coefficient c_z.

Fig. 11. Rigid case (medium gust): Streamwise and vertical force coefficients (solid lines) with the corresponding pressure force related parts (solid lines with symbols).

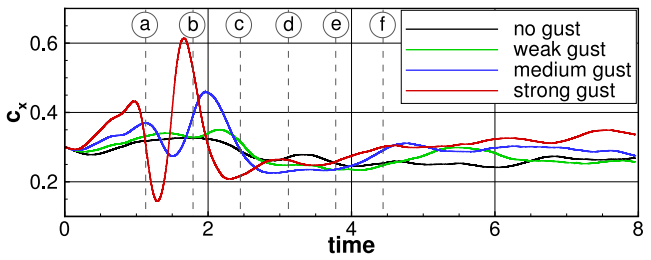

(a) Force coefficient c_x.

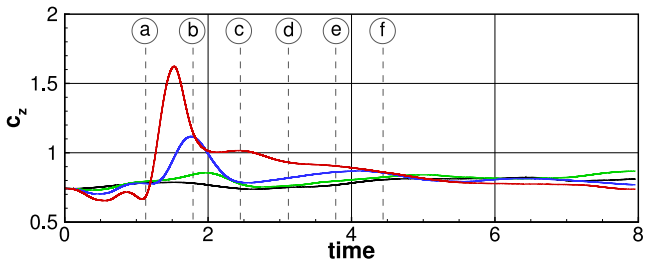

(b) Force coefficient c_z.

Fig. 12. Rigid case: Streamwise and vertical force coefficients predicted for different gust strengths.

streamwise and vertical force coefficients obtained for the flexible case and the *medium* gust with those predicted for the rigid case. The temporal evolutions of both cases are not identical, but also not so far from each other. Two findings can be derived from this observation. First, the deflection of the structure has a minor effect on these global surface-integrated quantities especially on the resulting peak values. Second, for highly unsteady FSI problems such a representation is insufficient. In that case instantaneous contour plots such as the streamwise velocity and the pressure are mandatory to apprehend the whole FSI phenomenon. Figs. 14 and 15 gather the distributions of u_1/u_∞ and $p/(\rho_{\text{air}} u_\infty^2)$ obtained by the FSI simulation relying on a FEM membrane discretization at the same six time instants as in Section 7.2. Again, a horizontal slice near the wall and a vertical slice located in the symmetry plane are chosen to depict the flow development. The position of the gust structure is tracked either by the iso-surface $u_1/u_\infty = 1.4$ or by its corresponding iso-line in the plane $y = 0$. The FSI-interface is gray with some lighting effects for a better representation of the membrane deflection.

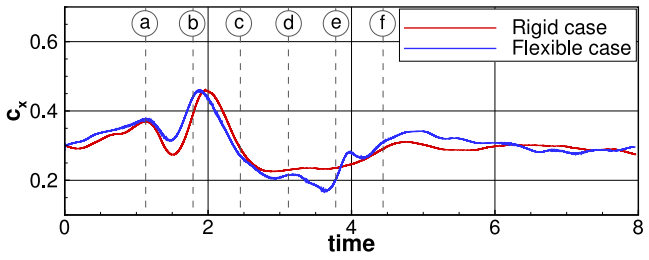

(a) c_x.

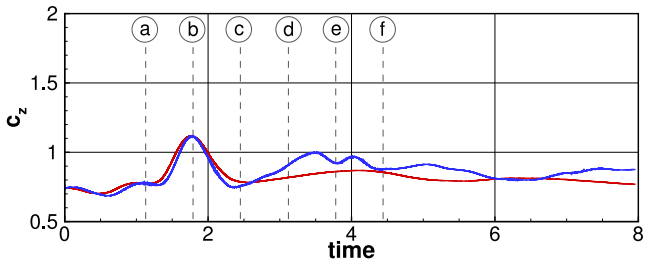

(b) c_z.

Fig. 13. Flexible FEM vs. rigid case (medium gust): Streamwise and vertical force coefficients.

To complete the visualization of the FSI phenomenon obtained for the *medium* gust, deflections of the membrane in the symmetry plane $y = 0$ are plotted in Fig. 16(b) for the same six time instants.

At the first time instant (Figs. 14(a) and 15(a)) the injection of the gust has just finished and it arrives at the flexible body. At this instant in time the membrane is already slightly deformed due to the loads of the turbulent flow without gust (see black line (a) in Fig. 16(b) and refer to De Nayer et al. (2018a) for more details). The gust at its current position has no significant effect on the deflection. Then, the gust moves downstream. At about $t^* \approx 1.8$ it hits the tip of the deformed membrane. As for the rigid case this time instant coincides with the maximum of the vertical force coefficient c_z (see Fig. 13(b)) due to the strong low pressure area above the hemisphere. However, this time the structure starts to deform (see red line (b) in Fig. 16(b)). Due to the impact of the gust, the front of the membrane grows hollow as visible in Figs. 14(b) and 16(b). In the indentation, a high pressure region is found (see Fig. 15(b)) and this zone is clearly larger than in the rigid case (see Fig. 9(b)). The gust structure continues to pass downstream and leaves the body. During this phase the forming indentation at the front still gets larger and deeper as depicted in Fig. 14(c) for $t^* \approx 2.45$ and with the blue line (c) in Fig. 16(b). Consequently, a certain delay between the maxima of the total forces at $t^* \approx 1.8$ and the maxima of the local deflections of the front is observed. In the next time instants the gust is convecting downstream in the wake and vanishes. The maximum of the deflection is reached in Fig. 14(c), when the gust has already passed the hemisphere completely. After this time instant the front indentation starts to decrease again (see green line (d) in Fig. 16(b)). Figs. 14(d) and 14(e) show how the passing of the gust into the wake strongly alters the recirculation area behind the hemisphere. Consequently, a pronounced and a relatively long phase, in which the streamwise force coefficient is lower than for the rigid case, is observed in Fig. 13(a). In this time interval an increase of c_z is found. An oscillation of the membrane front indentation occurs before it reaches its original deflected state again (see the evolution of the orange line (e) to the gray line (f) and then to the black line (a) (original state) in Fig. 16(b)). This phenomenon is responsible for the oscillation of the global force coefficients c_x and c_z observable in Figs. 13(a) and 13(b) at about $t^* \approx 3.8$. In the last time instant presented in Fig. 14(f) the gust has already vanished in the wake and the turbulent flow around the bluff body is back to the original state without gust. Consequently, the deflections of the inflated hemisphere return to their original level.

The injection of the wind gust occurs at an arbitrary time decided by the user. The wind gust is then superposed by the underlying turbulent fluctuations. In order to evaluate the effect of this injection time on the FSI phenomenon, five coupled FSI simulations applying different injection times are compared in Appendix.

7.3.2. Effect of varying gust strength

Gusts with different strengths are injected in front of the flexible structure. The force coefficients in streamwise and vertical directions obtained with the *weak*, *medium* and *strong* gusts are compared in Fig. 17. The force coefficients predicted for the different gusts on the flexible case look similar to those obtained for the rigid body. The histories of c_x only slightly differ concerning the amplitudes of the extrema. For the *strong* gust with the flexible body, c_x reaches a first local maximum of 0.460, then a local minimum of 0.245 followed by the second local maximum of 0.679. Considering

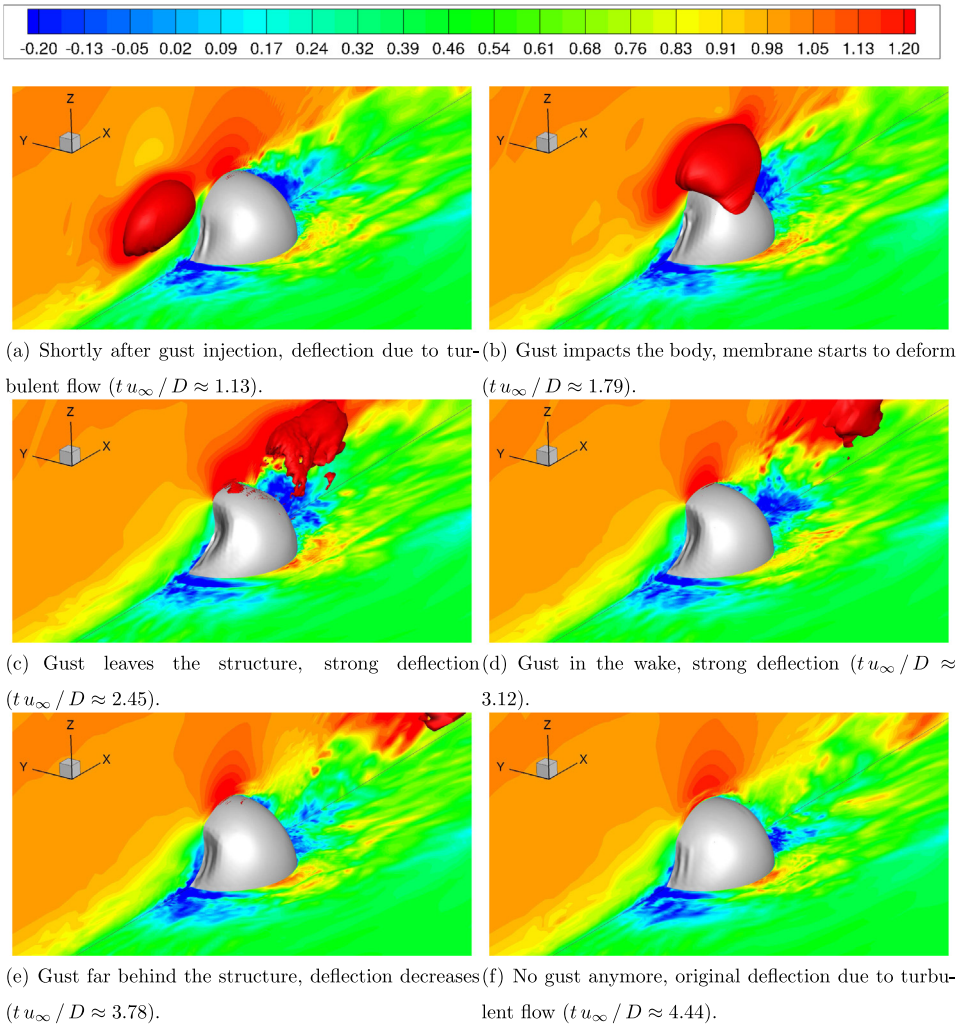

(a) Shortly after gust injection, deflection due to turbulent flow ($t\,u_\infty / D \approx 1.13$).

(b) Gust impacts the body, membrane starts to deform ($t\,u_\infty / D \approx 1.79$).

(c) Gust leaves the structure, strong deflection ($t\,u_\infty / D \approx 2.45$).

(d) Gust in the wake, strong deflection ($t\,u_\infty / D \approx 3.12$).

(e) Gust far behind the structure, deflection decreases ($t\,u_\infty / D \approx 3.78$).

(f) No gust anymore, original deflection due to turbulent flow ($t\,u_\infty / D \approx 4.44$).

Fig. 14. Flexible FEM case: Injected *medium* wind gust moving downstream and impacting an air-inflated flexible membrane in form of a hemisphere (streamwise velocity u_1/u_∞ in a slice near the bottom wall and in the symmetry plane $y = 0$). The gust structure is highlighted by an iso-surface of the streamwise velocity $u_1/u_\infty = 1.4$.

the rigid body, these extrema are 0.432, 0.144 and 0.614, respectively. Hence, the flexibility of the membrane tends to reduce the differences between the extrema, smoothing the slope of c_x. This is also valid for the *weak* and *medium* gusts.

Flow fields predicted for the *weak* and *strong* gusts are not plotted, since the spatial distributions of the streamwise velocity and the pressure do not really differ from those induced by the *medium* gust. Only their magnitudes change. However, a comparison of the corresponding structural deflections is of interest. Fig. 16 compares the deflections obtained for the *weak*, *medium* and *strong* gusts at the same six time instants as in Fig. 14. In case of the *weak* gust the indentation at the front increases until a deflection of minor amplitude is reached and, then, decreases with time (see Fig. 16(a)). In case of the *medium* and *strong* gusts, the deflections of the indentation are much larger and lead to waves along the vertical direction. This is visible in Figs. 16(b) and 16(c), where some lines cross each others.

A comparison of the maximally deflected membrane shapes is visualized in Fig. 18. Note that due to the time delays discussed above based on the histories of the forces, the maximal deflections observed for the three gust strengths are reached at different instants in time. Obviously, major changes are observed in the membrane deflections. As expected, the stronger the gust is, the deeper is the deflection at the front of the body (see Fig. 18). The formation of this indentation at the front has consequences on the rest of the structural shape: With increasing gust strength the tip of the body tends to be higher and the sides to be wider. These changes in the shape occur due to outer pressure distribution combined with the constant gauge pressure applied inside the closed volume. When the gust is far away, the indentation at the front reduces and the tip and sides of the hemispherical body return to their original positions.

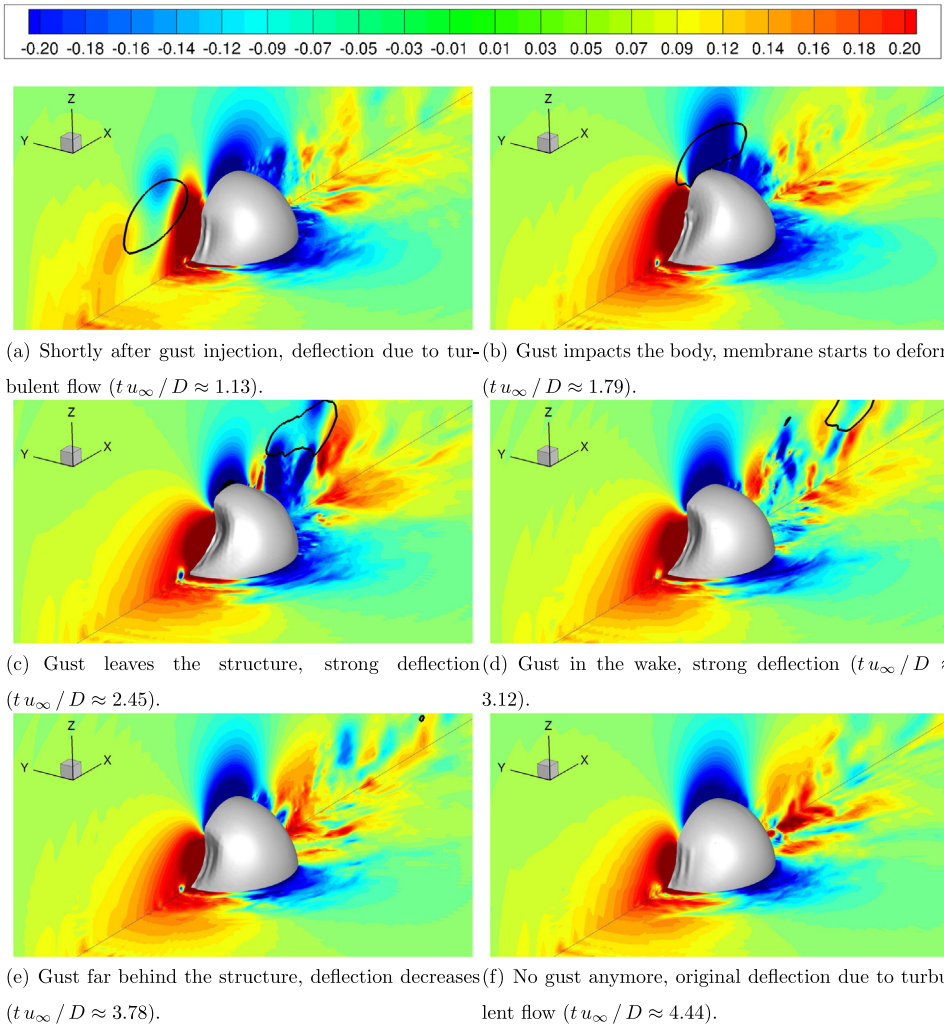

(a) Shortly after gust injection, deflection due to turbulent flow ($t\,u_\infty / D \approx 1.13$).

(b) Gust impacts the body, membrane starts to deform ($t\,u_\infty / D \approx 1.79$).

(c) Gust leaves the structure, strong deflection ($t\,u_\infty / D \approx 2.45$).

(d) Gust in the wake, strong deflection ($t\,u_\infty / D \approx 3.12$).

(e) Gust far behind the structure, deflection decreases ($t\,u_\infty / D \approx 3.78$).

(f) No gust anymore, original deflection due to turbulent flow ($t\,u_\infty / D \approx 4.44$).

Fig. 15. Flexible FEM case: Injected *medium* wind gust moving downstream and impacting an air-inflated flexible membrane in form of a hemisphere (pressure $p/(\rho_{\text{air}} u_\infty^2)$ in a slice near the bottom wall and in the symmetry plane $y = 0$). The gust position is highlighted by a black iso-line of the streamwise velocity $u_1/u_\infty = 1.4$ in the symmetry plane.

For a deeper analysis of the structural behavior and the possible failure of the material, the principal strain values ε_1 and ε_2 are computed according to:

$$\varepsilon_1, \varepsilon_2 = \frac{\varepsilon_{11} + \varepsilon_{22}}{2} \pm \sqrt{\left(\frac{\varepsilon_{11} - \varepsilon_{22}}{2}\right)^2 + \varepsilon_{12}^2} \ ,$$

where ε_{ij} stands for the covariant components of the Green–Lagrange strain tensor defined over the surface of each finite element. Fig. 19 depicts these principal strains for the maximally deflected structure at all three gust strengths. The maxima of ε_1 are found in all cases at the apex of the membranous structure, whereas the absolute values are augmented by a factor of about 1.75 between the weak and the strong gust. Note that in the case of the strong gust ε_1 reaches values of about 6.5% and thus slightly exceeds the recommended classical limit of 5% for the application of the St. Venant–Kirchhoff material model.

For the second principal strain ε_2 the minima are of interest. These appear at the border of the front indentation, which at least in the case of the strong gust partially coincides with the apex of the hemisphere. For this strain the extrema between the weak and the strong gust differ by a factor of about 2.7.

Furthermore, a classical criterion to analyze failure of ductile materials is to predict the von Mises stress and to compare this equivalent uni-axial tensile stress with the yield stress of the material. Fig. 20 depicts the distribution of the von Mises stress for the same instants in time which are shown for the principal strains in Fig. 19. In agreement with the first principal strain ε_1 the largest von Mises stresses are observed at the apex of the hemispherical membrane. Of course,

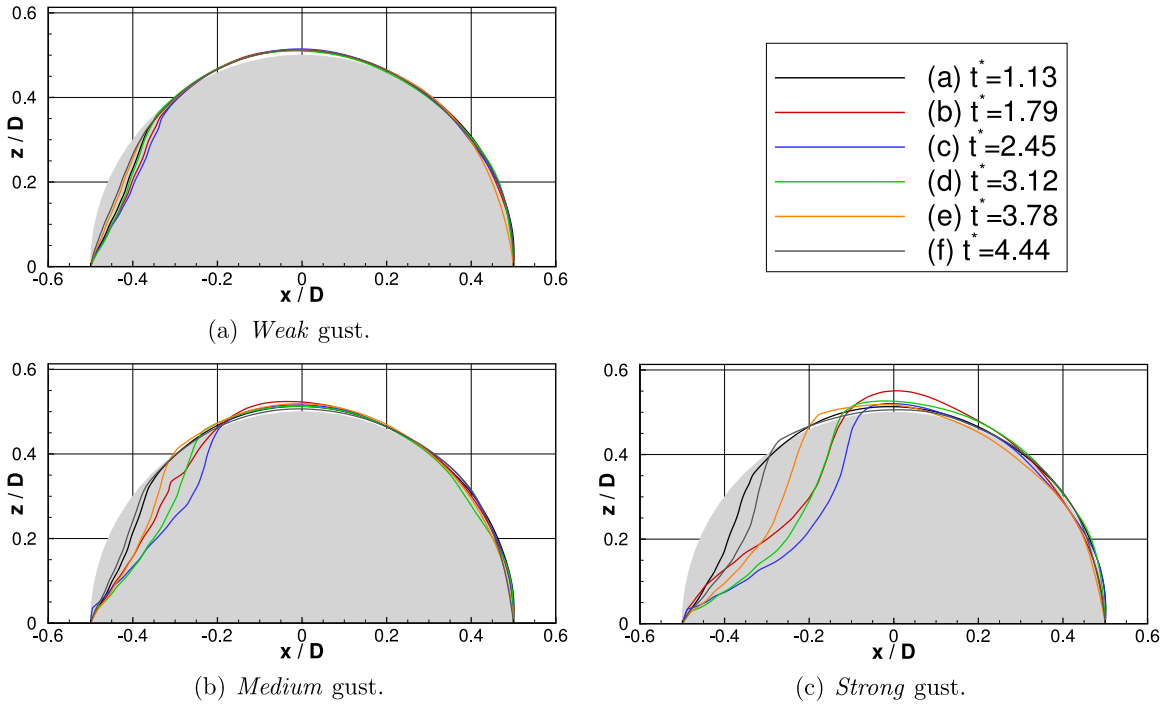

(a) *Weak* gust.

(b) *Medium* gust.

(c) *Strong* gust.

Fig. 16. Flexible FEM case: Structure deflections in the symmetry plane at six time instants.

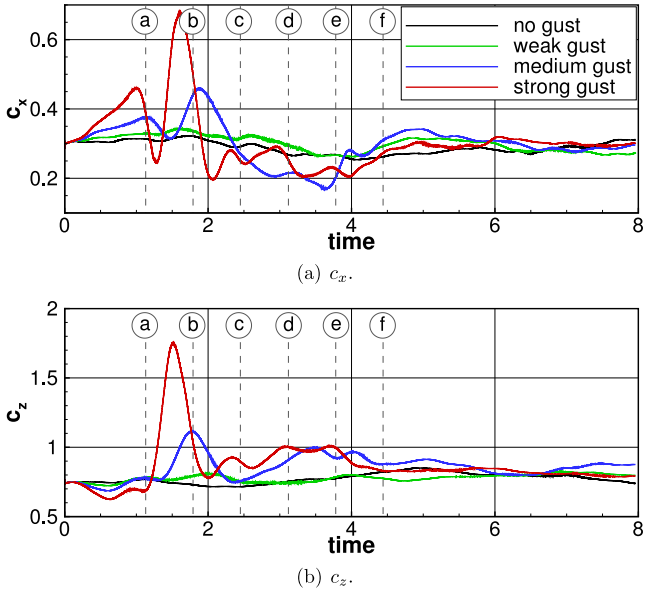

(a) c_x.

(b) c_z.

Fig. 17. Flexible FEM case: Streamwise and vertical force coefficients.

a rising gust strength leads to an increase of the von Mises stress, where again a factor of about 1.73 similar to ε_1 is found between the maxima of the weak and the strong gust. It has to be mentioned that in the present generic test case the von Mises stress does not reach the yield stress of silicone. According to the standardized plastic tensile test (EN ISO 527-2, ASTM D638) carried out in Wood et al. (2018) the yield stress is expected to be at least one order of magnitude higher than the currently occurring von Mises stress. Nevertheless, this issue does not play a role here, since the main purpose was to demonstrate that such kind of failure analysis is now possible for highly instantaneous loads acting on the structure.

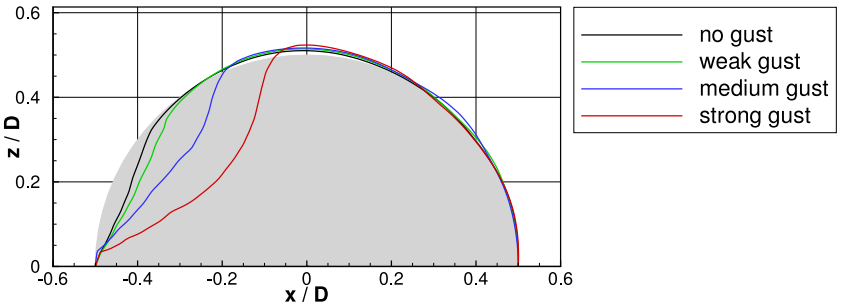

Fig. 18. Flexible FEM case: Maximum structural deflections in the symmetry plane for different gust strengths.

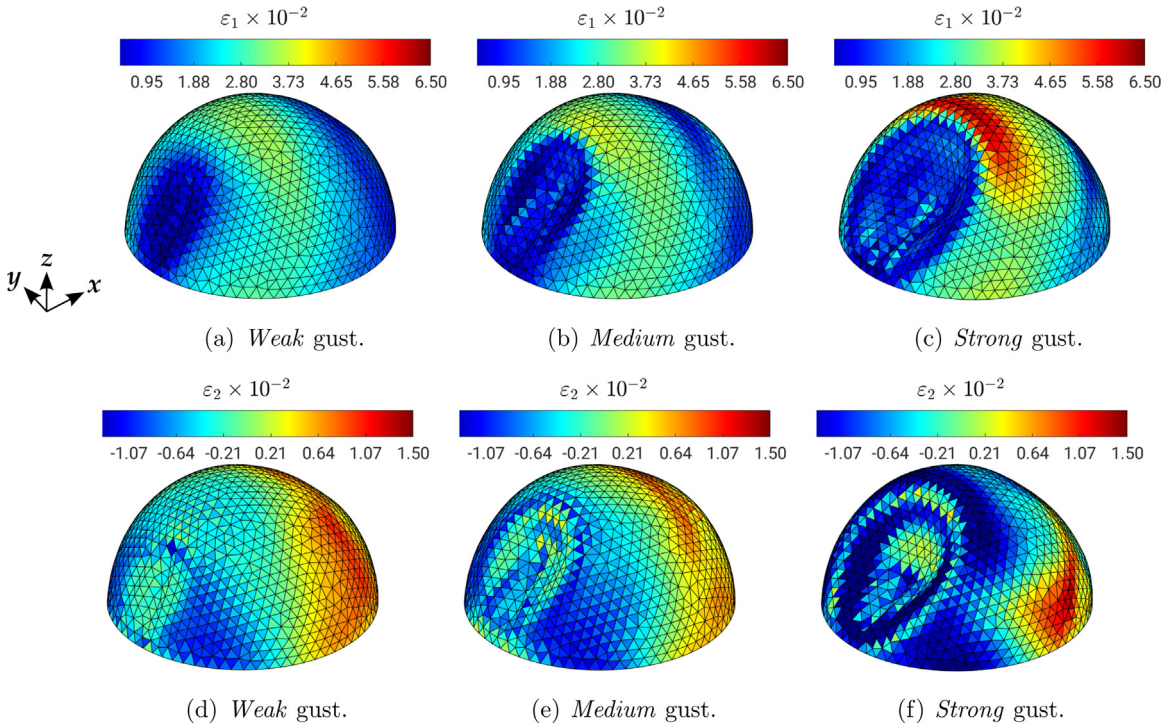

Fig. 19. Flexible FEM case: Distribution of the principal strain values ε_1 ((a) to (c)) and ε_2 ((d) to (f)) for the maximally deflected structure at different gust strengths.

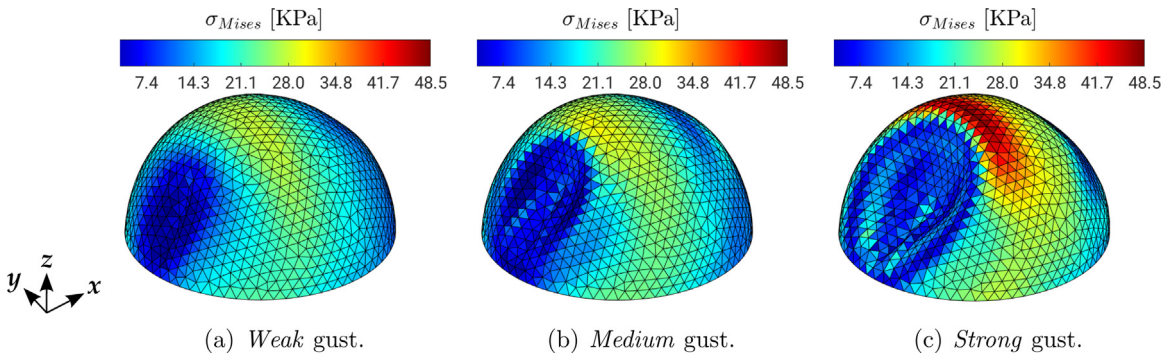

Fig. 20. Flexible FEM case: Von Mises stress distributions for the maximally deflected structure at different gust strengths.

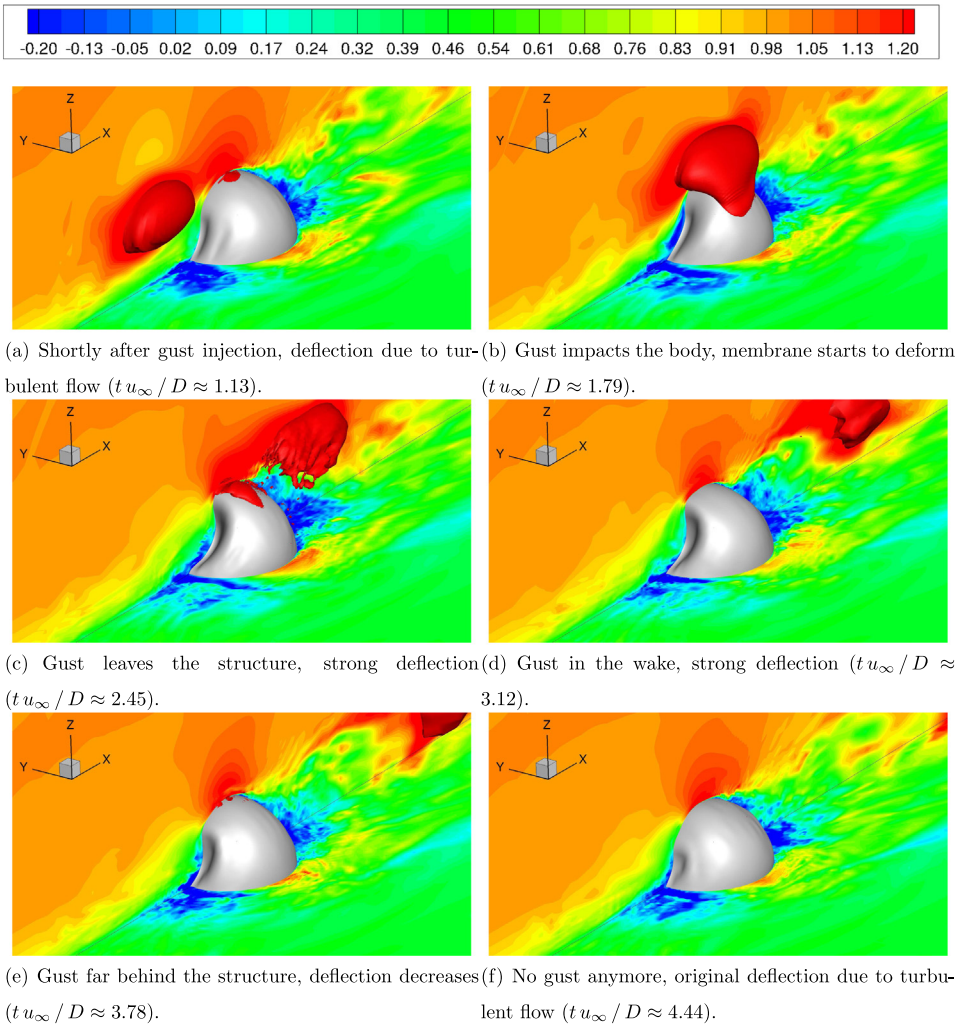

(a) Shortly after gust injection, deflection due to turbulent flow ($t\,u_\infty / D \approx 1.13$).

(b) Gust impacts the body, membrane starts to deform ($t\,u_\infty / D \approx 1.79$).

(c) Gust leaves the structure, strong deflection ($t\,u_\infty / D \approx 2.45$).

(d) Gust in the wake, strong deflection ($t\,u_\infty / D \approx 3.12$).

(e) Gust far behind the structure, deflection decreases ($t\,u_\infty / D \approx 3.78$).

(f) No gust anymore, original deflection due to turbulent flow ($t\,u_\infty / D \approx 4.44$).

Fig. 21. Flexible IGA case (medium gust) Injected *medium* wind gust moving downstream and impacting an air-inflated flexible membrane in form of a hemisphere (streamwise velocity u_1/u_∞ in a slice near the bottom wall and in the symmetry plane $y = 0$). The gust structure is highlighted by an iso-surface of the streamwise velocity $u_1/u_\infty = 1.4$.

7.3.3. FEM vs. IGA

As detailed in Section 5.2 the thin-walled structure is either discretized by finite elements or an IGA discretization. The results analyzed up to now are all based on the FEM discretization. The results of the IGA method are exemplarily shown in Fig. 21, which is the counterpart to Fig. 14. Obviously, both methods deliver very similar deflections of the membranous structure, where the main difference is found in the front indentation. In order to visualize this difference, the structural deflections along the symmetry plane obtained by IGA and FEM are plotted for the same six instants in time (see Fig. 22). For the first, fourth, fifth and sixth time instants the spatial evolution of the membrane predicted by IGA is very similar to its FEM counterpart. Small but rather visible differences appear for $t^* \approx 1.79$ and 2.45, where the deflections of the membrane are maximal. At $t^* \approx 1.79$ a kink in the deflections of the membrane predicted by FEM is present. Such artificial kinks are a consequence of the linear triangular membrane finite elements, which are large compared to the fluid cells at the FSI interface. In the case of large structural deflections, as those resulting from wind gust loading, the coarse low-order FEM mesh mapped to the fluid grid leads to an artificial roughness of the FSI interface. The coarser the FEM mesh is, the stronger is the artificial roughness (Apostolatos et al., 2019b). This artificial roughness can have a significant impact on the flow prediction, particularly on the location of the flow separation. Note that the FEM mesh currently employed for the FSI-LES simulation leads to flow predictions similar to those obtained by IGA as proved in Apostolatos et al. (2019b). Contrary to the FEM method, the isogeometric mortar-based mapping method predicts a smooth surface of the membrane (see Fig. 23(a)) since the artificial kinks arising from the FEM mesh (see Fig. 23(b)) are not transferred into the fluid domain. However, the IGA method leads to significantly higher computational costs as discussed in the next section.

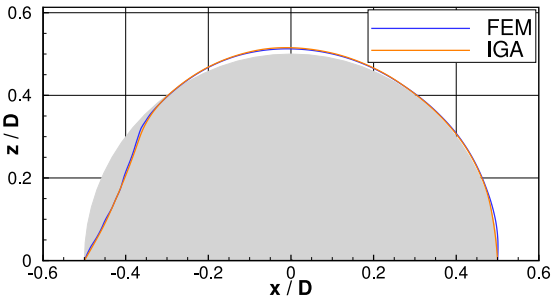

(a) Shortly after gust injection, deflection due to turbulent flow ($t\,u_\infty / D \approx 1.13$).

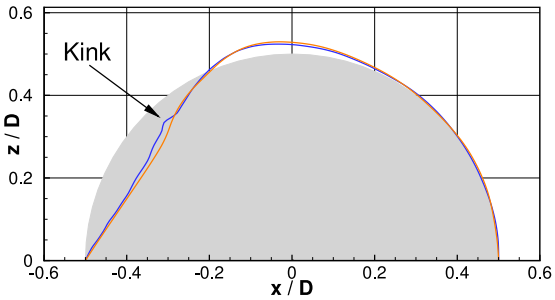

(b) Gust impacts the body, membrane starts to deform ($t\,u_\infty / D \approx 1.79$).

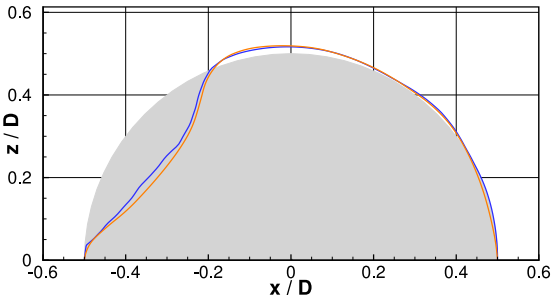

(c) Gust leaves the structure, strong deflection ($t\,u_\infty / D \approx 2.45$).

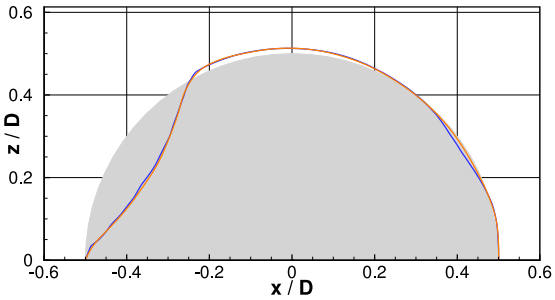

(d) Gust in the wake, strong deflection ($t\,u_\infty / D \approx 3.12$).

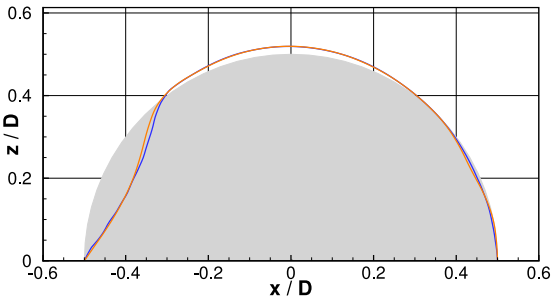

(e) Gust far behind the structure, deflection decreases ($t\,u_\infty / D \approx 3.78$).

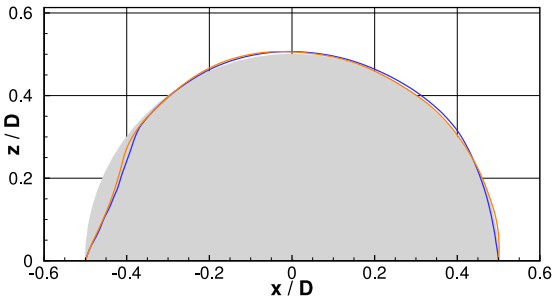

(f) No gust anymore, original deflection due to turbulent flow ($t\,u_\infty / D \approx 4.44$).

Fig. 22. Flexible IGA case vs. flexible FEM case: Structure deflections in the symmetry plane.

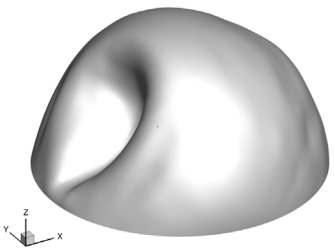

(a) IGA.

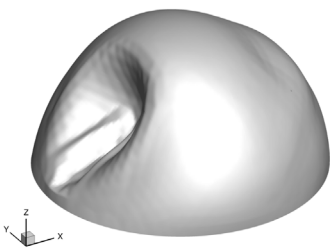

(b) FEM.

Fig. 23. Flexible IGA case vs. flexible FEM case: Deformed shape of the FSI interface at $t\,u_\infty/D \approx 2.45$.

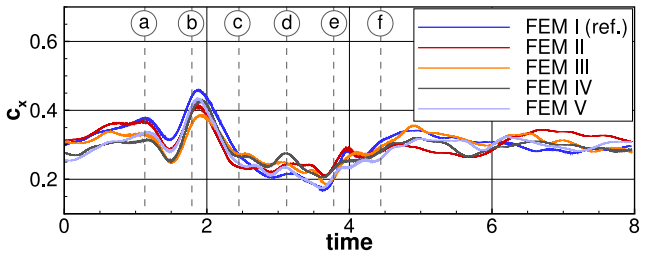

(a) c_x.

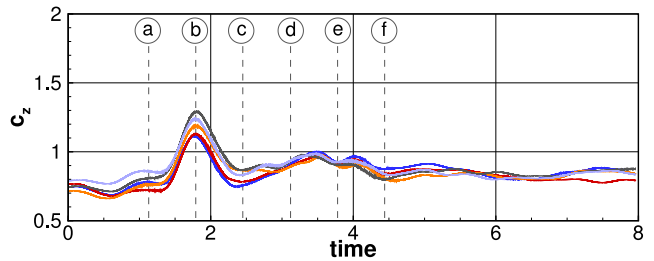

(b) c_z.

Fig. A.24. Flexible FEM case (medium gust): Streamwise and vertical force coefficients obtained with gusts injected at different time instants to demonstrate the effect of the underlying inflow turbulence.

7.4. Computational costs

The LES predictions including the different gusts conducted for the CFD case based on the rigid hemisphere took about 20 h wall-clock time on 40 processors (Intel Xeon Ivy Bridge E5-2650 with QDR Infiniband). The strength of the gust has a minimal impact on the computational costs (less than 0.5% of the total CPU time). The fully-coupled FSI-LES predictions including the gust and with a FEM discretization of the structure requires about 47 h on 42 processors of the same machine. This increase in CPU costs is only due to the FSI coupling (data exchange and fluid mesh adaption) and not due to the gust itself. The corresponding FSI-LES predictions applying the IGA discretization of the structure run during 230 h on 42 processors of the same machine. The total CPU-time increases about a factor of 5 compared to the FEM discretization. The IGA modeling alone is responsible for this strong increase and not the gust injection.

8. Conclusions

A recently developed novel gust injection technique was applied to simulate a challenging turbulent FSI case, i.e., a flexible membranous structure within a turbulent boundary layer undergoing highly transient wind events. The simulation methodology relies on a partitioned solution approach (LES/FEM/IGA) and takes the incoming turbulence into account. The purpose of this contribution was to show that an extension towards the consideration of wind gusts is straightforward and can be efficiently realized by the source-term formulation proposed in De Nayer and Breuer (2020), but up to now only validated based on laminar and turbulent background flows predicted on Cartesian grids. Similar to these generic test cases, the present real FSI application using a block-structured curvilinear grid confirms that it is possible to place the injection area of the gust close to the region of interest, which renders the method highly efficient. The numerical dissipation of the gust and time-consuming simulations for the transport of the gust from the inlet to the actual location of the FSI region are circumvented. Furthermore, the present practical application ratifies that the convergence behavior of the mass conservation equation does not deteriorate, since no source term is added to the continuity equation and thus the divergence-free condition for incompressible fluids is still satisfied. Consequently, a powerful methodology arises to tackle turbulent wind gusts in FSI applications.

The test case of the rigid and flexible hemisphere under different wind gust loads has brought the following findings:

- Horizontal wind gusts induce a significant increase of the forces in streamwise and vertical directions, i.e., a wind gust with an amplitude of $A_g = 1.5\,u_\infty$ already leads to a doubling of the global forces on the structure compared to the pure boundary layer flow.
- In the present case of the hemispherical structure the flexibility of the membrane slightly dampens the resulting peak values of the global forces compared to the rigid case.
- However, in case of the flexible structure the local fluid loads play a more important role than the global forces. In the current configuration the pressure force is identified as the dominant contribution and the shear force is only of minor importance.

- The pressure forces induced by the gust hitting the structure lead to strong local deflections especially on the front part but not exclusively. These deflections are found to appear with a certain delay with respect to the local and global forces.
- Based on the predicted deflections of the membrane it is possible to determine the local stresses and strains in the material. As a classical failure criterion for ductile materials the von Mises stress can be compared with the yield stress of the material in order to check the structural integrity.
- With the help of a fully-coupled FSI-LES prediction applying a FEM discretization for the structure, the safety of a design under the influence of highly transient wind events can be assessed in a time frame of less than two days on a small cluster.
- The same fully-coupled FSI-LES simulation including gust, but applying an IGA discretization of the membrane delivers similar results as the FEM one in terms of observed FSI phenomena, flow fields and deflections. As expected, the deformed shape of the membrane is smoother. However, the computational time is about five times higher.

CRediT authorship contribution statement

G. De Nayer: Conceptualization, Methodology, Software, Validation, Investigation, Visualization, Writing – original draft, Writing – review & editing. **M. Breuer:** Conceptualization, Methodology, Resources, Writing – original draft, Writing – review & editing, Supervision, Project administration, Funding acquisition. **K. Boulbrachene:** Conceptualization, Methodology, Investigation, Visualization, Writing – original draft, Writing – review & editing.

Declaration of competing interest

The authors declare that they have no known competing financial interests or personal relationships that could have appeared to influence the work reported in this paper.

Acknowledgments

The project is financially supported by the *Deutsche Forschungsgemeinschaft*, Germany under the contract number BR 1847/17-1. Additionally, the authors want to thank the Chair of Structural Analysis of the Technical University of Munich for providing the computational structure dynamics solver Carat++ (Bletzinger et al., 2006) and the open-source coupling software EMPIRE (Sicklinger et al., 2014). Finally, the authors are grateful to A. Apostolatos for his support on the post-processing.

Appendix. Reproducibility of the wind gust generation by the ST method

In order to evaluate the reproducibility of the wind gust generation by the ST method, five coupled FSI simulations with the FEM membrane discretization are carried out. In the reference simulation (denoted FEM I) discussed in the previous sections, the gust is injected directly after the restart, which continues the preceding simulation with continuous turbulent inflow fluctuations. In the other simulations (II to V) again the same restart file for the fluid flow and the structure as well as the turbulent inflow data are used. Thus, the initial conditions are identical to the reference simulation. The only difference is that the gusts are injected with a certain time delay of $\Delta t^*_{\text{delay}} = 1, 2, 3$ and 4 compared to the gust injection time of FEM I, respectively. Consequently, the same gust is superimposed on five different background flows allowing to evaluate the variation of the resulting forces as a result of these superpositions.

The predicted streamwise and vertical global force coefficients are compared in Fig. A.24. Note that in the figures the time axes for FEM II to V are accordingly shifted to fit the time of the reference simulation for the sake of a direct comparison.

Obviously, the histories of the force coefficients obtained for the five different cases differ in terms of the absolute values, whereas the instants in time at which the extrema appear are more or less the same. Nevertheless, visible differences in the extreme values of c_x and c_z can be observed. For example, the peak value of c_z varies between 1.11 (FEM I)and 1.29 (FEM IV), which is about 16% and thus not negligible. Variations of the same order of magnitude are visible for the streamwise force coefficient c_x. However, evaluating the differences between the local minima and the local maxima in the interval (a) to (c), the deviations are even stronger between $\Delta c_x = 0.123$ for FEM II and 0.175 for FEM IV. This observed variability requires deeper investigations and will be the topic of ongoing studies.

References

Adrian, R.J., 2007. Hairpin vortex organization in wall turbulence. Phys. Fluids 19 (4), 041301.

American Society of Civil Engineers, 1997. Standard Guidelines for Air Supported Structures. In: ASCE standard, American Society of Civil Engineers, URL https://books.google.de/books?id=srVxQgAACAAJ.

Apostolatos, A., Bletzinger, K.-U., Wüchner, R., 2019a. Weak imposition of constraints for structural membranes in transient geometrically nonlinear isogeometric analysis on multipatch surfaces. Comput. Methods Appl. Mech. Engrg. 350, 938–994.

Apostolatos, A., De Nayer, G., Bletzinger, K.-U., Breuer, M., Wüchner, R., 2019b. Systematic evaluation of the interface description for fluid–structure interaction simulations using the isogeometric mortar-based mapping. J. Fluids Struct. 86, 368–399.
Augier, B., Bot, P., Hauville, F., Durand, M., 2012. Experimental validation of unsteady models for fluid structure interaction: Application to yacht sails and rigs. J. Wind Eng. Ind. Aerodyn. 101, 53—66.
Bailly, C., Comte-Bellot, G., 2015. Turbulence. Springer.
Basar, Y., Weichert, D., 2013. Nonlinear Continuum Mechanics of Solids: Fundamental Mathematical and Physical Concepts. Springer Science & Business Media.
Bletzinger, K.-U., Wüchner, R., Kupzok, A., 2006. Algorithmic treatment of shells and free form-membranes in FSI. In: Bungartz, H.-J., Schäfer, M. (Eds.), Fluid-Structure Interaction. In: Lecture Notes in Computational Science and Engineering, LNCSE, vol. 53, Springer, Heidelberg, pp. 336–355.
Boulbrachene, K., De Nayer, G., Breuer, M., 2021. Assessment of two wind gust injection methods: Field velocity vs. split velocity method. J. Wind Eng. Ind. Aerodyn. 218, 104790.
Breitenberger, M., Apostolatos, A., Philipp, B., Wüchner, R., Bletzinger, K.-U., 2015. Analysis in computer aided design: Nonlinear isogeometric b-rep analysis of shell structures. Comput. Methods Appl. Mech. Engrg. 284, 401–457.
Breuer, M., 2018. Effect of inflow turbulence on an airfoil flow with laminar separation bubble: An LES study. Flow Turbul. Combust. 101 (2), 433–456.
Breuer, M., De Nayer, G., Münsch, M., Gallinger, T., Wüchner, R., 2012. Fluid-structure interaction using a partitioned semi-implicit predictor-corrector coupling scheme for the application of large-eddy simulation. J. Fluids Struct. 29, 107–130.
Burton, T., Sharpe, D., Jenkins, N., Bossanyi, E., 2001. Wind Energy Handbook. John Wiley & Sons.
De Nayer, G., Apostolatos, A., Wood, J.N., Bletzinger, K.-U., Wüchner, R., Breuer, M., 2018a. Numerical studies on the instantaneous fluid–structure interaction of an air–Inflated flexible membrane in turbulent flow. J. Fluids Struct. 82, 577–609.
De Nayer, G., Breuer, M., 2014. Numerical FSI investigation based on LES: Flow past a cylinder with a flexible splitter plate involving large deformations (FSI-PfS-2a). Int. J. Heat Fluid Flow 50, 300–315.
De Nayer, G., Breuer, M., 2020. A source-term formulation for injecting wind gusts in CFD simulations. J. Wind Eng. Ind. Aerodyn. 207, 104405.
De Nayer, G., Kalmbach, A., Breuer, M., Sicklinger, S., Wüchner, R., 2014. Flow past a cylinder with a flexible splitter plate: A complementary experimental-numerical investigation and a new FSI test case (FSI-PfS-1a). Comput. & Fluids 99, 18–43.
De Nayer, G., Schmidt, S., Wood, J.N., Breuer, M., 2018b. Enhanced injection method for synthetically generated turbulence within the flow domain of eddy-resolving simulations. Comput. Math. Appl. 75 (7), 2338–2355.
Durst, F., Schäfer, M., 1996. A parallel block-structured multigrid method for the prediction of incompressible flows. Int. J. Numer. Methods Fluids 22 (6), 549–565.
Frost, W., Long, B.H., Turner, R.E., 1978. Engineering Handbook on the Atmospheric Environmental Guidelines for Use in Wind Turbine Generator Development. Tech. rep., Tennessee Univ., Tullahoma (USA). Space Inst.; National Aeronautics and Space Administration, Huntsville, AL (USA). George C. Marshall Space Flight Center.
Glück, M., Breuer, M., Durst, F., Halfmann, A., Rank, E., 2003. Computation of wind-induced vibrations of flexible shells and membranous structures. J. Fluids Struct. 17 (5), 739–765.
Heinrich, R., Reimer, L., 2013. Comparison of different approaches for gust modeling in the CFD code TAU. In: Int. Forum on Aeroelasticity & Structural Dynamics 2013. URL https://elib.dlr.de/85834/.
IEC-Standard, 2002. 61400-21. Tech. report.
Kareem, A., Wu, T., 2013. Wind-induced effects on bluff bodies in turbulent flows: Nonstationary, non-Gaussian and nonlinear features. J. Wind Eng. Ind. Aerodyn. 122, 21–37.
Kasperski, M., 2007. A consistent model for the codification of wind loads. J. Wind Eng. Ind. Aerodyn. 95 (9), 1114–1124.
Klein, M., Sadiki, A., Janicka, J., 2003. A digital filter based generation of inflow data for spatially–developing direct numerical or large–eddy simulations. J. Comput. Phys. 186, 652–665.
Kwon, D.K., Kareem, A., 2013. Generalized gust-front factor: A computational framework for wind load effects. Eng. Struct. 48, 635–644.
Lesieur, M., 2008. Turbulence in Fluids, 4th edition Springer.
Michalski, A., Gawenat, B., Gelenne, P., Haug, E., 2015. Computational wind engineering of large umbrella structures. J. Wind Eng. Ind. Aerodyn. 144, 96–107.
Michalski, A., Kermel, P.D., Haug, E., Löhner, R., Wüchner, R., Bletzinger, K.-U., 2011. Validation of the computational fluid–structure interaction simulation at real-scale tests of a flexible 29 m umbrella in natural wind flow. J. Wind Eng. Ind. Aerodyn. 99 (4), 400–413.
Mokin, N.A., Kustov, A.A., Trushin, S.I., 2017. Numerical simulation of an air-supported structure in the air flow. In: Bletzinger, K.-U. and Onate, E. and Kröplin, B. (Eds.), VIII Int. Conf. on Textile Composites and Inflatable Structures, Structural Membranes 2017.
Newman, B.G., Ganguli, U., Shrivastava, S.C., 1984. Flow over spherical inflated buildings. J. Wind Eng. Ind. Aerodyn. 17 (3), 305–327.
Norris, S.E., Cater, J.E., Stol, K.A., Unsworth, C.P., 2010. Wind turbine wake modelling using large-eddy simulation. In: Proceedings of the 17th Australian Fluid Mechanics Conference. Curran Associates, Inc., University of Auckland, Australia.
Pasquetti, R., Peres, N., 2015. A penalty model of synthetic micro-jet actuator with application to the control of wake flows. Comput. & Fluids 114, 203–217.
Philipp, B., Wüchner, R., Bletzinger, K.-U., 2016. Advances in the form-finding of structural membranes. Procedia Eng. 155, 332–341.
Piomelli, U., Chasnov, J.R., 1996. Large–eddy simulations: Theory and applications. In: Hallbäck, M., Henningson, D.S., Johansson, A.V., Alfredson, P.H. (Eds.), Turbulence and Transition Modeling. Kluwer, pp. 269–331.
Santo, G., Peeters, M., Van Paepegem, W., Degroote, J., 2020. Fluid-structure interaction simulations of a wind gust impacting on the blades of a large horizontal axis wind turbine. Energies 13, 509.
Schlatter, P., Orlu, R., Li, Q., Brethouwer, G., Fransson, J.H.M., Johansson, A.V., Alfredsson, P.H., Henningson, D.S., 2009. Turbulent boundary layers up to $Re_\theta = 2500$ studied through simulation and experiment. Phys. Fluids 21 (5), 51702.
Schmidt, S., Breuer, M., 2017. Source term based synthetic turbulence inflow generator for eddy–resolving predictions of an airfoil flow including a laminar separation bubble. Comput. & Fluids 146, 1–22.
Sen, S., De Nayer, G., Breuer, M., 2017. A fast and robust hybrid method for block-structured mesh deformation with emphasis on FSI-LES applications. Int. J. Numer. Methods Eng. 111 (3), 273–300.
Sicklinger, S., Belsky, V., Engelmann, B., Elmqvist, H., Olsson, H., Wüchner, R., Bletzinger, K.-U., 2014. Interface Jacobian-based co-simulation. Int. J. Numer. Methods Eng. 98 (6), 418–444.
Singh, R., Baeder, J.D., 1997. Direct calculation of three-dimensional indicial lift response using computational fluid dynamics. J. Aircr. 34 (4), 465–471.
Smagorinsky, J., 1963. General circulation experiments with the primitive equations I: The basic experiment. Mon. Weather Rev. 91 (3), 99–165.
Thompson, J.F., Warsi, Z.U.A., Wayne Mastin, C., 1985. Numerical Grid Generation: Foundations and Applications, Vol. 45. North-Holland.
Wales, C., Jones, D., Gaitonde, A., 2014. Prescribed velocity method for simulation of aerofoil gust responses. J. Aircr. 52 (1), 64–76.
Wang, T., Wüchner, R., Sicklinger, S., Bletzinger, K.-U., 2016. Assessment and improvement of mapping algorithms for non-matching meshes and geometries in computational FSI. Comput. Mech. 57 (5), 793–816.
Wood, J.N., Breuer, M., De Nayer, G., 2018. Experimental studies on the instantaneous fluid–structure interaction of an air–Inflated flexible membrane in turbulent flow. J. Fluids Struct. 80, 405–440.

Wood, J.N., De Nayer, G., Schmidt, S., Breuer, M., 2016. Experimental investigation and large-eddy simulation of the turbulent flow past a smooth and rigid hemisphere. Flow Turbul. Combust. 97 (1), 79–119.
Wu, Y., Sun, X., Shen, S., 2008. Computation of wind-structure interaction on tension structures. J. Wind Eng. Ind. Aerodyn. 96, 2019–2032.
Wüchner, R., Kupzok, A., Bletzinger, K.-U., 2007. A framework for stabilized partitioned analysis of thin membrane-wind interaction. Int. J. Numer. Methods Fluids 54 (6–8), 945–963.
Yuan, C., Puyong, W., Xianlong, J., 2010. Dynamic analysis of flexible container under wind actions by ALE finite-element method. J. Wind Eng. Ind. Aerodyn. 98, 881–887.